Evaluation of the physical properties of experimental macromolecular crowding systems

by

© Venketesh Thrithamara Ranganathan

A thesis submitted to the School of Graduate Studies in partial fulfillment of the requirements for the degree of Doctor of Philosophy.

Department of Physics and Physical Oceanography
Memorial University

April 2022

St. John's, Newfoundland and Labrador, Canada

Abstract

Biological cells are crowded environments consisting of both large and small molecules. The macromolecular crowding observed in biological cells is likely very important to the structure and function of a living cell. Since the macromolecules can interact with each other, this makes the system complex and there remain several open questions. In the laboratory, artificial crowder molecules can be used to create experimental model systems that mimic the cellular environment. Artificial crowders such as the polysaccharide, Ficoll, have long been assumed to be compact and colloidal, but a holistic understanding of its structure and dynamics is lacking.

This thesis investigates the structure of Ficoll using multiple experimental techniques. We report rheology, small angle neutron scattering, self diffusion and relaxation measurements using nuclear magnetic resonance experiments on two widely used artificial crowder molecules, Ficoll-70 and Ficoll-400. Our results, combining measures of structure, diffusion, relaxation and rheology, show that Ficolls are more *polymer like* than colloid like. Importantly, we find that the self-diffusion of HDO molecules in the suspension is an efficient probe to evaluate volume occupancy of the suspension under investigation. We then evaluate the physical properties of a protein crowder solution, BSA, and phytoglycogen, a natural plant based dendrimer using the methods developed to evaluate the Ficoll suspension properties.

For all crowders, we find that the self diffusion coefficient decreases exponentially with a characteristic concentration of 10-12 wt %. We also observe that the NMR transverse relaxation of the solvent is a sensitive, independent measure of water confinement, which can be correlated with suspension rheology and self diffusion. To summarize, the highlight of this thesis is that structural and dynamical methods that report on macromolecules *as well as* solvent can provide a more complete view of macromolecular crowding.

To my beloved parents Mrs. Annapurneswary and Mr. Ranganathan

Lay summary

All living species are made up of biological cells. A tiny microscopic biological cell can contain macromolecules up to concentrations of 300 - 400 $\frac{g}{L}$, traditionally thought to occupy 30-40 % of the total volume of the cell. Under these crowded conditions, the molecular properties are affected by the spatial constraints imposed by other molecules. In this thesis, we investigate the structure and hydration properties of laboratory model crowder molecules which are used to mimic crowding conditions in a living biological cell. Despite extensive research in macromolecular crowding the physical structure and the hydration properties of simple crowders, such as the polysaccharide Ficoll, are not yet well understood. Here we employ multiple experimental techniques, rheology, small angle neutron scattering and nuclear magnetic resonance spectroscopy, to extract the structure and hydration properties of widely-used Ficoll crowder molecules. We further extend our study to a protein crowder, BSA, and phytoglycogen, a plant based dendrimer nanoparticle.

Acknowledgements

I thank Dr. Anand Yethiraj, my thesis supervisor, for his guidance on research work and thesis completion. His support and directions during the research term at CNRS, France and NIST, USA are highly valued. In professional terms, I have learned the importance of scientific collaborations and its impact, research presentation in layman language, scientific writing and multi-tasking from him. My special voice of thanks for offering his time to discuss my personal grounds and guiding me with appropriate actions and suggestions.

I thank my supervisory committee members Dr. G. Todd Andrews and Dr. Stefan Wallin for evaluating my annual progress and approving my performances in each year of my PhD. Also, I thank Dr. Stefan Wallin and his student Saman Bazmi for their useful research discussions.

My sincere thanks to Dr. Mike Morrow, who has been instrumental in developinalgorithmicg my understanding on nuclear magnetic resonance spectroscopy and I express my joy in carrying out experiments in the laboratory that with Dr. Morrow share with us.

My sincere thanks to my colleagues Dr. Swomitra Palit, Shivani Semwal, and Yanitza Trosel Arroyo for their valuable research discussions. I thank all the wonderful team at the Physics main office. On a special note, I would like to express my sincere thanks to Donna Geraldine Coombs and Maureen Wade. A notable thanks to Lisa O'Brien, an outstanding role-model who has inspired me in professional development.

I express my sincere thanks to Dr. Yun Liu, NIST, USA for training me to operate the small angle neutron scattering instrument for data collection and for his immense support during our experiment at NIST. My sincere thanks to Dr. Francesco Piazza, CNRS, France, for accepting me as his project student and Dr. Josef Hamacek for

providing access to his laboratory and guiding me in the project work.

The phytoglycogen nanoparticles used in this thesis were a kind gift from Dr. Phil Whiting (Mirexus Biotechnologies Inc.). Sincere thanks to Dr. John Dutcher (founder Mirexus Biotechnologies) for encouraging us to examine phytoclogen nanoparticles *via* diffusion NMR.

I thank the Reslife team of Memorial University for playing a key role in elevating my leadership skills and providing professional training to make me fit to the role I handle as a residence coordinator. The path of my supervisor, Dwayne Taverner, and residence life advisors Cory Flynn, Travis Myers, Julie Goudie, Simon Erlich stays as a clear root in heading to true leadership. Also, my sincere gratitude goes to the RC team for providing me a wonderful environment to work with.

I thank my instructor for English Shobha (HSST), who has arranged several interaction platforms, which aided me to overcome my communication barriers. I express my sincere gratitude to Subhashini (HSST) for inspiring me to aspire to a career in physics. My special thanks to Suresh sir who torch guided my academics and motivated me to pursue higher goals.

I would like to thank Professor Divya D, Government Victoria College, Palakkad, for being a source of tremendous support, guidance and motivation. To aspire to a career in physics, in professional and personal life, her influence on each of my steps will ever be cherished with highest gratitude. I thank Dr. Dillip Kumar, Indian Institute of technology, Madras and Dr. Ranjini Bandyopadhyay, Raman Research Institute, Bangalore for supervising me in soft-matter physics research.

I thank Dr. Sunish Kumar (Ulster University, Belfast, UK) and Ramya for their support and guidance in arts and science. I also express my sincere thanks to Anupama Geneshan (RN, Eastern Health) & Mohammad Yazar (RN, Eastern Health), Mini Nair & Jayasankar Vatathoor, Dr. Prem Kumar (Memorial University) & Swapna prem, Smitha & Pradeep, Krishnamoorthy (St. John's) who have played key roles in my PhD term. A special thanks to Muna Smith Yethiraj for his artistic advice on the table of content preparation to represent our understanding of the structure of Ficoll investigated in my thesis.

I express my since thanks to Sabari (Biocon, Bangalore), Abhijith, Sri Hari Puthanpurayil (University of Oklahoma), Sujit Embrandiri, Jamseena and Asif, Abinu Jyothini, Deepu & Anju, Janani Shivasankar, Adhersh Radhakrishnan, Gagandeep Nagra and Akhil Joji for their unique contributions in my professional and personal development. With pride, I express my heartfelt thanks to Andaladimanakkal Unni Namboothiri and Vishnu Namboothiri, as well as my source of motivation and support, Vellinezhy Harikrishnan.

I feel prestige to thank Moozhikulam Harikrishnan and Vishnudev K S whose art and talent has pronounced influence in my academic and non academic performances. My special thanks to Thrithamara Grama Jana Samooham. I thank Seshamani Master (Late) with whom I have got excellent opportunity to work and receive guidance. Thanks to Suresh T S, Sekhar T S, Rajesh & family, and Krishnaraj P K for their support, to take up higher studies in physics. Dr. Keerthi Thirtamara Rajamani and Dr. Nanditha Anandakrishnan have significantly contributed to my academic progress. Nirmala Ravi (Late), Dr. Sreevidya Lagisetty, Dr. Nagaanand will be ever remebered with highest gratitude. My sincere thanks to both of them. I would like to show my due respect to my maternal & paternal family members for their unbounded care on my personal and professional growth.

While I am still far behind fulfilling the essential needs of my parents, confidence is no less, I will fulfill it in near future. Keeping immense gratitude as a strong foundation, I target to achieve heights to serve them right. My mother Annapurneswary and father Ranganathan, as well as my sister Anitha Kaushik, my brother-in-law Kaushik and the little one Harishankar, all will be ever respected with most gratitude. I also thank my in-laws and family. Last but not least, I thank my wife Sandhya for being an integral part of my progress and our little one Hridya T Venketesh.

Table of contents

List of tables

List of figures

Chapter 1

Introduction

1.1 Colloids

Colloids are heterogeneous systems in which particles of size ranging from nanometer (nm) to micrometer (μm) are dispersed in a continuous medium that is liquid, gas or solid [1]. Toothpaste, food, pharmaceuticals, ceramics, personal care products and paint are some examples of colloids that we encounter in our daily life. Owing to the size of the colloidal particles, the effects of gravity on the dispersed particles are negligible while thermal effects are predominant in determining dispersion properties. Thermal motion of solvent molecules sets up collisions with the dispersed particles resulting in their random motion, termed as Brownian motion [2]. Colloidal suspensions exhibiting Brownian dynamics are often used to model complex systems that are subject to the action of multiple potentials acting simultaneously. In systems like a living biological cell, each molecule is under the simultaneous action of multiple intermolecular and intramolecular forces [3]. Understanding the properties of individual macromolecules and their influence in sustaining the cellular life cycle, therefore, remains challenging. In-vitro studies of macromolecular colloidal suspensions through a bottom up approach, where the complexity can be systematically enhanced, are an efficient method to develop understanding on these complex systems. This chapter underlines different colloidal interactions, provides an introduction to macromolecular crowding observed in living cells, the underlying theme of this thesis, and further discusses the goal of the thesis.

1.2 Interactions in colloids

1.2.1 Excluded-volume interaction

The presence of a particle or molecule makes its true volume inaccessible for other particles or molecules to occupy. The prevention of overlap between two particles leads to a short range repulsion, and is often modelled as hard spheres. This is referred to as the excluded-volume interaction [4]. This is an entropic interaction, and it can have a significant impact on the properties of the system, especially at high volume occupancy. The associated free energy is proportional to the difference of the logarithms of the partition functions with and without the excluded volume interactions imposed [5]. Assume that we have ω number of boxes and we impose that each box can have only one molecule, the partition function, $Z_{excluded}$ is the number of ways we can choose N boxes to place the indistinguishable molecules. Mathematically,

$$Z_{excluded} = \frac{\omega!}{N!(\omega - N)!} \tag{1.1}$$

Without the excluded volume condition imposed, the partition function is,

$$Z = \frac{\omega^N}{N!} \tag{1.2}$$

Assuming $\omega \gg$ N, the difference in free energy, $\Delta G_{excluded}$ is

$$\Delta G_{excluded} = -k_B T ln \frac{Z_{excluded}}{Z} = k_B T \frac{N^2}{\omega} = N k_B T \phi. \tag{1.3}$$

k_B is the Boltzmann constant, T is the temperature, $\frac{N}{\omega}$ is the number density, which is proportional to the volume fraction ϕ [5]. The above equation states that the excluded volume interaction increases the difference in free energy of the system that is proportional to ϕ.

1.2.2 Depletion interaction

Consider a suspension of particles with different sizes, for instance, a bidisperse colloidal suspension. In such systems, the small particle cannot occupy the space between two large particles when the large particle surfaces are separated by a distance that is smaller than the small particle diameter as shown in Figure 1.1. However, the free volume for small particles will increase as the large particles approach closer. The entropy-driven attraction between the large particles in a polydisperse system is known as the depletion attraction.

Consider two particles in a box of volume V_{box}, contained in a unit cell of volume ν (lattice model). The free energy change induced by excluded volume interactions can be written as [5]

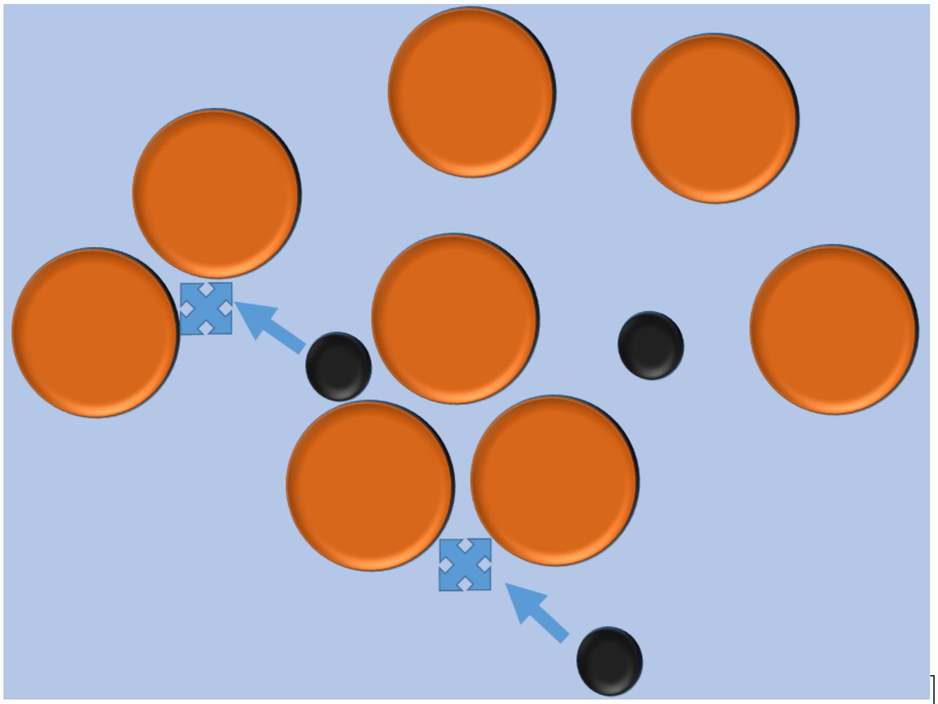
]

Figure (1.1) The small particle cannot occupy the space between two large particles when the large particle surfaces are separated by a distance that is smaller than the small particle diameter, leading to the depletion attraction.

$$
\begin{aligned}
\Delta G_{ex} &= -Nk_BT\ln\left(\frac{V_{\text{box}} - V_{\text{excluded}}}{\nu}\right) + Nk_BT\ln\left(\frac{V_{\text{box}}}{\nu}\right) \\
&= -Nk_BT\left[\ln\left(\frac{V_{\text{box}} - V_{\text{excluded}}}{\nu}\right) - \ln\left(\frac{V_{\text{box}}}{\nu}\right)\right] \\
&= -Nk_BT\ln\left(1 - \frac{V_{\text{excluded}}}{V_{\text{box}}}\right).
\end{aligned} \tag{1.4}
$$

Using $V_{\text{excluded}} << V_{\text{box}}$ and the relation $\ln(1-x) \approx -x$, we get

$$
\Delta G_{ex} = Nk_BT\left(\frac{V_{\text{excluded}}}{V_{\text{box}}}\right). \tag{1.5}
$$

Now, consider two large spherical particles of radius R in a sea of small spherical particles of radius r. For each of the large particles, there is a volume $\frac{4}{3}\pi(R+r)^3$

that is unavailable to the centre of mass of a small particle [5]. When the center-to-centre separation between the large spheres, d, is less than $2(R+r)$, an overlap of the excluded volume develops as the large particles approach closer than $2(R+r)$. Now the excluded volume for the small particles is given by [5],

$$V_{\text{excluded}} = 2\frac{4\pi}{3}(R+r)^3 - V_{\text{overlap}} \tag{1.6}$$

where $V_{\text{overlap}} = \frac{2\pi}{3}\left(R+r-\frac{d}{2}\right)^2\left(\ 2R+2r+\frac{d}{2}\ \right)$, where d is the distance between the centers of the two spheres. The depletion force can be obtained by substituting equation 1.6 in equation 1.5 and taking its negative partial derivative with respect d as

$$F_{\text{depletion}} = -\frac{\partial G_{\text{ex}}}{\partial d} = -\frac{Nk_BT\pi}{V}\left[\left(R+r\right)^2 - \frac{d^2}{4}\right] \tag{1.7}$$

Thus the depletion force is proportional to the concentration, $c = \frac{N}{V}$, where N is the number of molecules in unit volume V.

1.2.3 The van der Waals attraction

The interaction arising from fluctuating electric fields of dipoles results in an attraction between the particles that is known as the van der Waals attraction. An electrically neutral atom can have an electric dipole moment due to a small relative shift in the center of the positive nucleus and the center of electron clouds. The atom A induces a dipolar interaction with the second near by atom, B, with an interaction energy of [6]

$$E_{\text{vdw}} = p_B E_A(r) \tag{1.8}$$

where E_A is the electric field of atom A, p_B is the dipole moment of the atom B, and r is the distance of the dipole from atom A. Since p_B is proportional to r^{-3}, E_{vdw}

is proportional to r^{-6}. This interaction is for point particles. For spherical colloidal particles, the interaction energy is obtained by integrating over two sphere volumes, and one gets [7]

$$E = \frac{-A_h}{6}\left[\frac{R_1 R_2}{(R_1 + R_2)l}\right] \tag{1.9}$$

where A_h is the Hamaker constant, R_1 and R_2 are the radius of the spheres, and l is the separation between their surfaces.

1.2.4 Electrostatic interactions

If a colloidal dispersion contains charged particles or ions, the electrostatic interaction plays a vital role in determining the colloidal structure and phases. The charged particles are equivalent to macro-ions. In a suspension of particles having ionizable groups, the ions dissociate in solution to form the electric double layer. They interact via a screened Coulomb repulsion. The counterions of opposite charge to that of the particle maintains the overall electrical neutrality of the dispersion. In a mean-field (Boltzmann) approximation, the spatial dependence of the counter ion distribution is given by [4]

$$n_i(r) = n_i(0)\exp\left(-\frac{z_i e V(r)}{k_B T}\right). \tag{1.10}$$

where $n_i(0)$ is the bulk concentration of ith species, z_i is the valancy of ith ion species and e is the electronic charge. The potential obeys the Poisson-Boltzmann equation,

$$\nabla^2 V(r) = -\frac{zen(r)}{\epsilon\epsilon_0}. \tag{1.11}$$

The solution under the Debye-Hückel approximation ($\sinh(\theta) = \sin\theta$) yields

$$V(r) = \frac{q^2\exp(-\kappa r)}{\epsilon\epsilon_0 r}, \tag{1.12}$$

where $\kappa^{-1} = \left[\frac{2z^2e^2n_0}{\epsilon\epsilon_0 k_B T}\right]^{-\frac{1}{2}}$ is known as the Debye screening length. The Debye screening length for 0.1 M phosphate buffer solution used to disperse BSA protein in our study is 0.7 nm [8].

1.3 Diffusion of colloidal particles

At thermal equilibrium, solvent molecules exhibit random motions resulting from collision with the colloidal particles. These collisions, in turn, set the colloidal particle in random motion called diffusion. Consider a particle in a viscous medium under the action of random collision forces, F_r. The equation of motion is given by,

$$F_r = \frac{md^2x}{dt^2} + \zeta v_x \tag{1.13}$$

where the frictional coefficient $\zeta = 6\pi\eta R_h$ for a spherical object with hydrodynamic radius R_h. Multiplying Equation 1.13 with x on both sides and writing $\frac{xd^2x}{dt^2}$ as $\frac{d}{dt}(x\frac{dx}{dt} - (\frac{dx}{dt})^2)$ and $\zeta x\frac{dx}{dt}$ as $\frac{\zeta}{2}\frac{dx^2}{dt}$ equation 1.13 takes the form

$$\frac{\zeta}{2}\frac{dx^2}{dt} = xF_r - m\left(\frac{d}{dt}\left[x\frac{dx}{dt}\right] - \left[\frac{dx}{dt}\right]^2\right) \tag{1.14}$$

$$\frac{\zeta}{2}\frac{dx^2}{dt} = xF_r - m\left(\frac{d}{dt}\left[xv\right] - v^2\right) \tag{1.15}$$

The quantities, F_r and x, as well as x and v are uncorrelated. Thus those terms vanishe in a statistical averaging of the above equation resulting in

$$\zeta\frac{d\langle x^2\rangle}{dt} = 2m\langle v^2\rangle. \tag{1.16}$$

In one dimension, the right hand side of the above equation is k_BT, from the equipartition theorem, and upon integrating, one can show that

$$\langle x^2 \rangle = \frac{2k_BT}{\zeta}t. \tag{1.17}$$

In 3 dimensions,

$$\langle r^2 \rangle = \frac{6k_BT}{\zeta}t = 6Dt. \tag{1.18}$$

The constant $D = \frac{k_BT}{\zeta}$ is called the diffusion coefficient of the colloidal particle. For a sphere of hydrodynamic radius R_h, D=$\frac{k_BT}{6\pi\eta R_h}$ The hydrodynamic radius is more generally used for macromolecules in solution, and is the radius of a sphere that diffuses as the macromolecule does in dilute solution.

1.4 Polymers in the dilute and semi-dilute-regime

Polymers exhibit concentration-dependent static and dynamical properties [9, 10, 11]. In the dilute limit, the osmotic pressure obeys the van't Hoff law and depends linearly on the concentration. The relative viscosity in this regime also depends linearly on concentration, c [12]. In the semi-dilute limit, the osmotic pressure π exhibits scaling of the form $c^{\frac{9}{4}}$. The osmotic compressibility, $\chi \sim \frac{\partial \pi}{\partial c}^{-1}$, thus scales as $c^{-\frac{5}{4}}$ [13]. The viscosity, on the other hand, is expected to scale as $c^{\frac{15}{4}}$ in this regime [14, 15]. Cohen *et al.* [16] showed that a phenomenological form of osmotic pressure can describe behaviour spanning the dilute and semi-dilute regime, and showed that the cross-over form $\pi = Ac + Bc^{\frac{9}{4}}$ described the experimental results well. This in turn yields a form for the osmotic compressibility $\chi = D/(1 + \alpha c^{\frac{5}{4}})$ where $D = \frac{1}{A}$ and $\alpha = \frac{9B}{4A}$.

1.5 Macromolecular crowding

In both the intracellular and extracellular space of a biological cell, multiple macromolecules exist at a high concentration of about 300 - 400 $\frac{g}{L}$. The effect of the environment on the structure and motions of individual molecules is known as macromolecular crowding. The protein content in a human cell is about $340\frac{g}{L}$ [17], haemoglobin exists at a concentration of about 350 $\frac{g}{L}$ [18] in red blood cells, and the mitochondrial matrix has protein contents up to 500 $\frac{g}{L}$ [19]. Due to the physical and chemical properties of different molecules in a crowded environment, each molecule is subject to the action of multiple potentials. However, regardless of the presence of any physical forces which drive attraction or repulsion, such as the effects of electrostatics or hydrodynamics, the excluded volume is the fundamental interaction in macromolecular crowding [20]. The relative sizes of the molecules is the basis for the non-specific steric repulsion leading to excluded volume interactions. In Figure 1.2, (a), the presence of molecules in a given volume and remaining available free volume for a much smaller test molecule is shown. The Figure 1.2 (b), indicates the excluded volume for test molecule of similar size to the molecules in the environment. In a suspension of probe particle of radius r_p and crowder molecules $r_{crowder}$, a covolume can be defined as the volume of a sphere with radius, $r_c = r_p + r_{crowder}$ [21].

In order to understand crowding effects, there can be two different approaches, the bottom-up approach and the top-down approach. In the bottom-up approach, experiments are performed with hard-sphere model crowder molecules and then one can systematically increase the complexity of the crowded environment. In the top-down approach, one would begin the investigation with an intact cell and then simplify [23]. While facilitating the systematic introduction of complexity, the bottom-up approach allows controlling a wide range of physiologically relevant parameters like

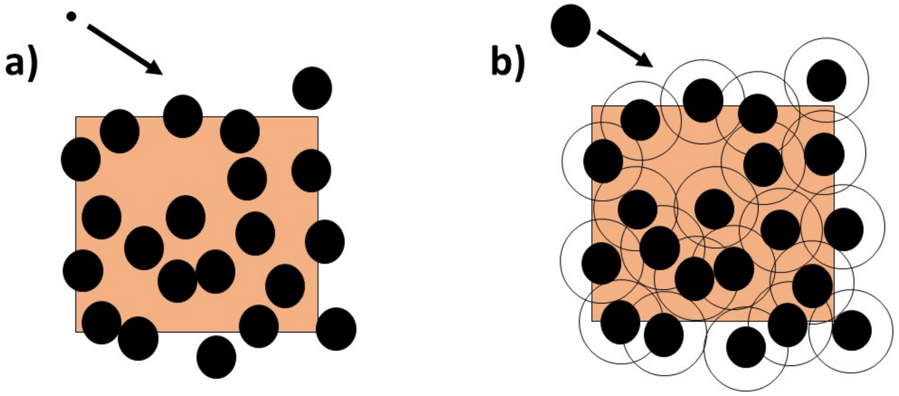

]

Figure (1.2) (a) In a volume where molecules occupy 30% of the space, the remaining 70% is available for other molecules. The free volume is shown in yellow. (b) A molecule of similar size, however, can not approach to the space beyond the region indicated by open circles. The free volume available here is much smaller [22].

pH of the system, temperature, ionic concentration, and molecular sizes, to name a few. This aids in the better understanding of features of living systems such as structure, dynamics, self-assembly, intermolecular and intramolecular interactions, folding and unfolding kinetics of proteins and aggregation behaviour [24, 25].

Stagg *et al.* report that the conformations of a globular charged protein, apoflavodoxin from the bacterium *desulfovibrio desulfuricans* is dependent on its environment at neutral pH [26]. They observe an increase in the secondary structure in the native state of apoflavodoxin and enhanced stability, induced by the crowding agent, Ficoll-70, a polysucrose macromolecular crowder. In an another study [27], they show that irrespective of the initial configuration of proteins, crowding, with dextran as the crowding agent, accelerates proteins' folding dynamics. Palit *et al* [28] report in a combined pulsed field gradient nuclear magnetic resonance and small angle neutron scattering study that a significant polymer chain compression occurs when the crowder size is much smaller than the polymer size. They do not observe compression when the probing polymer and crowder sizes are comparable. Shin *et al.*, find in their simulation study that large crowder molecules enhance the chain looping dynamics for a given polymer chain when compared with small crowder molecules, an explicit effect of excluded volume interactions [29].

Muramatsu *et al.* in their study of diffusion of four different tracer proteins of different molecular weights in four different globular proteins as crowder molecule with simple hard-sphere approximations, observe reduction in diffusion of tracer molecules of several orders when background protein concentration reaches about 200 $\frac{g}{L}$ [30]. Palit *et al.* in an investigation on the diffusion of poly(ethylene glycol), PEG, in a model hard-sphere crowder, Ficoll-70, show a 10 to 100 times enhancement in the relative mobility of the PEG compared with the crowding agent Ficoll-70 in the crowding limit, indicating that the PEG polymer's flexibility assists diffusion through interstitial spaces between crowder molecules [31]. Further, they report that while the crowder's charge enhances the polymer diffusion at intermediate crowder concentration, the crowder charge does not significantly impact polymer diffusion at crowding concentration. In a test study on the influence of the artificial crowders, Ficoll and dextran, on the stability of a protein, cytochrome, towards heat perturbation, structure and shape, Christiansen *et al.* summarize that probe molecule size, shape, folding and unfolding routes, crowder size, shape and charge are some important parameters that determine the net effect of macromolecular crowding [32]. Pielak *et al.* comment that while considering the stabilizing action of excluded volume interactions, one has to account for the intermolecular and intramolecular non-specific interaction of crowder molecules in predicting the influence of crowding [33].

The above studies are just a few examples from the literature. The available literature on the effects of excluded volume on the conformations of various probe molecules of different physical and chemical properties are abundant [34, 35, 36, 37]. However, the implicit assumption is an excluded volume that mimics the picture in Figure 1.2, i.e a solid (and possibly spherical) crowder molecule. A well-used artificial crowding agent has been the Ficoll particle, a nanometer-scale highly branched but crosslinked polysaccharide macromolecule. In spite of its extensive use, there has not been a systematic examination on the structure of the Ficoll molecule. To fill this existing void in macromolecular crowding research, we investigate the structure, hydration and flow properties of Ficoll-70 and Ficoll-400 polysucrose molecules. Further, we compare the dynamics and hydration properties of these molecules with bovine serum albumin, a protein crowder and phytoglycogen suspensions in this thesis.

1.6 Crowders for bottom-up studies

The hard sphere (HS) potential is a well-used model for inter-crowder interactions in crowding studies. It is defined by an infinite repulsion at distances smaller than the contact distance, σ, between two particles and no interaction at all when particles are not in contact. The infinite potential on surface contact arises from incompressible nature of the particles. Figure 1.3 shows the interaction potential energy and force as a function of distance r for hard spheres of diameter σ. At $r = \sigma$ both the energy and forces rises to ∞ from 0.

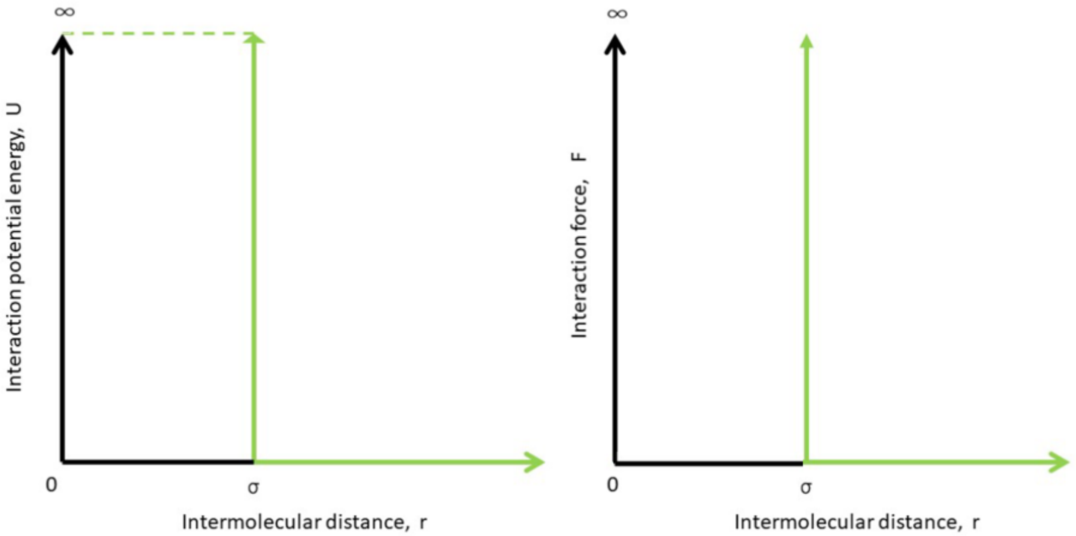

Figure (1.3) Interaction potential energy and interaction force as a function of distance for hard sphere interactions [38].

The hard-sphere model is very successful in predicting many interesting features of crowding. For instance, the hard-sphere model predicts the thermodynamical activity coefficient, a measure of solute-solute interactions, seen in protein solutions at physiological conditions [39]. An extended hard sphere model is, on the other hand, is used to understand the colligative properties (i.e the generic concentration dependent properties) of globular proteins [40]. However, in the two-state protein folding equilibrium, the HS model is unreliable in free energy predictions since the protein has various conformations beyond a rigid rod-like structure [41]. By extension, the examination of the structure of the crowder molecule is essential before predicting their effects on probe molecules under crowding.

Wenner *et al* in their study of binding affinity and catalytic rate of the restriction enzyme EcoRV with DNA under crowding conditions, with Ficoll-70 as the crowding agent, report that the covolume increases up to 2.5 % w/V and then decreases until 10 % w/V and then remains constant [21]. Further addition of Ficoll-70 does not show any decrease in covolume indicating that Ficoll further squeezes to keep covolume constant [21]. Rusinga *et al* report that Ficoll is rather a highly crosslinked polymer mesh whose interior resembles a semi-dilute suspension of short polymer chains [42]. In their study, they propose that at 300 $\frac{g}{L}$ of Ficoll-70, ACTR, an acid tolerance regulatory protein with helical as well as a random coil intrinsically disordered protein (IDP), infiltrates into the Ficoll, destabilizing the helical structure of the IDP. They argue that it is possible because the Ficoll has ample solvent filled space in aqueous dispersion. They conjecture that as the Ficoll concentration is increased to 400 $\frac{g}{L}$, the Ficoll mesh squeezes and the intra-mesh becomes inaccessible for IDP chains and the IDPs are forced to confine in the interstitial space between Ficoll spheres. In an another study, Biswas *et al.* observed that the microviscosities of mixture of Dextran-70 (molecular weight 70 kDa) and Ficoll-70 (molecular weight 70 kDa) are higher than the microviscosities of their individual solution [43]. They propose that the enhanced microviscosity of the mixture of crowding agent arises due to the entanglement of Ficoll-70 and dextran [43]. Experiments by Fissell *et al.* reveal that Ficoll penetrates pores smaller than its size [44].

These studies suggest, in direct and indirect ways, that Ficoll is more complex than a rigid particle; they raise questions on the applicability of Ficoll molecules as model hard-sphere crowders. Nevertheless, a systematic study solely focusing on the structure of Ficoll, its hydration properties and dynamics has not yet been reported. This thesis reports the detailed experimental investigation of structure of Ficolls of two different sizes, Ficoll-70 (M_W = 70 kDa) and Ficoll-400 (M_W = 400 kDa) examined by rheological measurements, and two independent modalities of nuclear magnetic resonance spectroscopy, along with small angle neutron scattering experiments of Ficoll-400. The effects of crowding on the conformation and chemical kinetics of probe molecules depends on the properties of the crowding agent such as shape and size of the crowder molecule.

Distinct crowding agents such as bovine serum albumin (BSA) and Ficoll are often used to study the protein folding and refolding kinetics [45], amyloid formation of lysozyme [46], and to evaluate quinary interactions, an interaction that mediates the formation of dynamic complexes under crowding [47]. Questions about the nature of the crowder are not restricted to Ficoll. As an example, Roosen-Runge *et al.* showed that the globular protein has a structure that can be modelled by an ellipsoidal colloid [48], while Sarangapani *et al.* establish limits for a colloidal picture for globular proteins [49, 50]. Considering the extensive use of the protein crowder molecule BSA, we perform a comparison of the BSA suspension properties with that of the artificial crowder molecule Ficoll.

Unlike Ficoll, a synthetic polysaccharide, phytoglycogen is a naturally occurring plant based polysaccharide molecule [51]. A SANS study by Dutcher and coworkers indicates that the phytoglycogen is a hard-sphere-like colloid. By performing quasielastic neutron scattering, they quantify the water content in the phytoglycogen particles and study their hydration dynamics [51]. In this thesis, we also investigate the concentration dependent self diffusion coefficient of phytoglycogen and water, as well as the NMR transverse relaxation of water molecules in aqueous suspensions of phytoglycogen nanoparticles.

1.7 Thesis structure

In Chapter 2, a detailed discussion on various experimental techniques used in this thesis is described. Chapter 3 reports the complementary views of Ficoll structure using multiple techniques. Chapter 4 reports a comparison study, via nuclear magnetic resonance (NMR), of bovine serum albumin and phytoglycogen. Chapter 5 summarizes and provides conclusions for our experimental studies and future directions.

Chapter 2

Experimental techniques

2.1 Nuclear magnetic resonance spectroscopy.

The search for nuclear magnetic resonance (NMR) originated in 1930. Gorter, from the Netherlands, reported attempts to observe a ^1H NMR signal in $KAl(SO_4)_2 12H_2O$ [52] using a calorimetric technique. He, however, could not succeed in his attempt, presumably due to poor signal to noise ratio [52]. Using a 0.2T magnet, Felix Bloch successfully measured the NMR signal for protons in water around 1945. Also, surprisingly, he observed that the T_1-relaxation for water is of the order of seconds, which until then was thought to be of the order of years [52]. In 1952, Bloch and Purcell received the Nobel prize for the discovery of NMR. Stejskal and Tanner thereafter introduced the concept of pulsed field gradient NMR (PFG-NMR). Karger *et al* used this method to measure the molecular diffusion coefficient in a porous material, zeolite. The application of NMR spectroscopy then started expanding to different zones of research and one of the important inventions is magnetic resonance imaging, independently developed by Lauterbur [53], Damadian [54] and Mansfield [55].

Some nuclei possess an intrinsic property called nuclear spin angular momentum (which does not have any classical analog). Associated with this nuclear spin angular momentum there will be a nuclear spin magnetic moment. That is, the nucleus acts as a tiny magnet with the strength represented by its magnetic moment vector. When placed in an external magnetic field, the net magnetization vector, which is the statistical average of individual magnetic moments, will align parallel to the external field, B. It has to be noted that the individual spins still can point in random directions due to the thermal motion of the nucleus but the net magnetization vector aligns in the direction of the external field. If this bulk magnetization is set to an angle β with respect to the external magnetic field, the vector will start to precess about the magnetic field. This precession is called *Larmor precession* and the frequency with which it rotates is called *Larmor frequency*. The rotation of the magnetization vector from its equilibrium alignment is the key that we use to generate an NMR signal. A radio frequency (RF) pulse of Larmor precession frequency helps in manipulating the rotation of magnetization vector from the equilibrium.

When subjected to an external magnetic field, a spin-$\frac{1}{2}$ nucleus, for instance, the proton, ${}^1H$, will have two spin states, $|\alpha\rangle$, the spin up, lower energy state and $|\beta\rangle$, the spin down, higher energy state. In an ensemble of spin-$\frac{1}{2}$ nuclei, if a measurement is made, the system will collapse to one of its eigenstates. The eigenvalues for spin-$\frac{1}{2}$ nuclei are $m = \frac{1}{2}$ and $m = -\frac{1}{2}$, i.e. if the z component of spin angular momentum is measured, the measurement results in one of its eigenstates with corresponding eigenvalue. Mathematically,

$$I_z\psi_m = \pm m\hbar\psi_m. \tag{2.1}$$

Quantum mechanics restricts the transition between the two states by selection rules, which states that the m can only change in steps of 1. The transition from the lower energy state $|\alpha\rangle$, with eigenvalue $m = \frac{1}{2}$ to higher energy state $|\beta\rangle$, with eigenvalue, $m = -\frac{1}{2}$ and vice versa, are, therefore, the only allowed transitions. When placed in an external magnetic field of strength B, the magnetic moment μ will interact with the external field. The energy of interaction is $E = -m\hbar\ \gamma B$, where γ is the gyromagnetic ratio of the nucleus. The energy corresponding to the transition between the $|\alpha\rangle$ to $|\beta\rangle$ is $E = \hbar\gamma B = \hbar\omega_L$ where ω_L is the Larmor frequency. This is the same frequency with which the bulk magnetization vector rotates when placed in a magnetic field at an angle β. If a radio frequency (RF) pulse of the same frequency as the Larmor precession frequency is applied in a direction perpendicular to the bulk magnetization, the magnetization vector tilts to an angle that depends on the time duration at which the RF pulse is applied. Manipulation of the rotation and relaxation of the magnetization vector are key to how different NMR experiments are designed.

2.1.1 Frame of reference

The bulk magnetization vector precesses around the external magnetic field according to the vector model (chapter 4 in ref [56]). Introduction of a rotating frame of reference simplifies the vector analysis. Consider a frame of reference that is rotating at the same frequency as the Larmor precession frequency. In this rotating frame, the magnetization vector appears to be stationary. If the frequency of rotation of the rotating frame is slightly different from the Larmor frequency, then the offset frequency, Ω is,

$$\Omega = \omega_L - \omega_{frame} \tag{2.2}$$

Then the reduced field in the rotating frame will be,

$$\Delta B = -\frac{\Omega}{\gamma} \tag{2.3}$$

Apart from reducing the mathematical time dependent complexities, the concept of the rotating frame hints that an RF field of strength much less than the external magnetic field can manipulate the rotation of the bulk magnetization in the rotating frame.

2.2 NMR Experiments

2.2.1 Longitudinal (T_1) and transverse (T_2) relaxation

When first rotated from equilibrium and then on removal of the perturbation, the magnetization vector returns to equilibrium (in the direction of the magnetic field along the z-axis) with a time duration τ. The duration with which the longitudinal component reaches back to the equilibrium is the T_1 relaxation time.

The T_1 relaxation can be measured using the inversion recovery pulse sequence. The magnetization vector rotates by π when an RF pulse is applied in the perpendicular (x-axis) direction of external field for a certain duration of time (in our experiments it is 20 μs). On the removal of the RF pulse, the magnetization vector relaxes to its equilibrium state and a $\frac{\pi}{2}$ pulse (an RF pulse of half the duration) is applied to detect the signal in the detection (xy) plane. The time between the two pulses is progressively increased (with τ typically varied from tens of milliseconds to seconds) to obtain the signal intensity as a function of the time between the pulses. The pulse sequence, known as the inversion recovery pulse sequence is shown in Figure 2.1. The intensity of the magnetization vector at any time τ is

$$M_z(\tau) = M_0\left(1 - 2\exp\left(-\frac{\tau}{T_1}\right)\right). \tag{2.4}$$

In equation 2.4, T_1 is the longitudinal relaxation time.

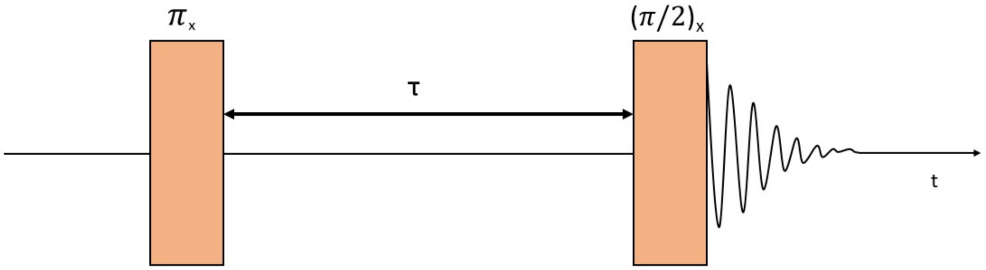

Figure (2.1) Inversion recovery NMR pulse sequence

There is a second kind of relaxation process in NMR, relating to the loss of coherence in the in-plane transverse component of the magnetization. This is known as T_2 relaxation. We measure T_2 relaxation using the spin echo (SE) pulse sequence. In an SE experiment a $\frac{\pi}{2}$ RF pulse is first applied along the x-axis which rotates the magnetization vector to the -y-axis. after which the magnetization precesses in the xy-plane. However due to local field inhomogeneities, some spins precess faster and some precess slower than the Larmor frequency, resulting in the spread of vectors in the xy-plane and thus a loss of phase coherence in the signal. After a time τ, a π RF pulse is applied along either the x-axis or y-axis, which inverts the phase accumulated during the period between the initial pulse and the π pulse. A schematic of the pulse sequence is shown in figure 2.2. At a time τ after the π pulse, the vector spread at time τ is completely canceled and phase coherence is briefly regained. This is the spin echo. We obtain the T_2 relaxation time by repeating the SE sequence shown in Figure 2.2 with a variable delay time τ between the pulses, and fitting the magnetization to

$$M_y(\tau) = M_0 \exp\left(\frac{-\tau}{T_2}\right) = M_0 \exp\Big(-\tau R_2\Big) \tag{2.5}$$

where $R_2 = \frac{1}{T_2}$ is the transverse relaxation rate. Figure 2.3 depicts the growth of the longitudinal magnetization M_z in an inversion recovery test (left) and, the decay of the transverse magnetization M_{xy} in an SE experiment (right). The intermolecular dipolar interaction is a likely mechanism for T_2 relaxation. Molecular tumbling results in local fluctuations of magnetic field, which in turn affects the field of nearby dipoles. This interaction, in turn, affects the rotational motion of the neighbouring molecules, which occur on the picosecond-to-nanosecond time scale [58]. The rotational correlation

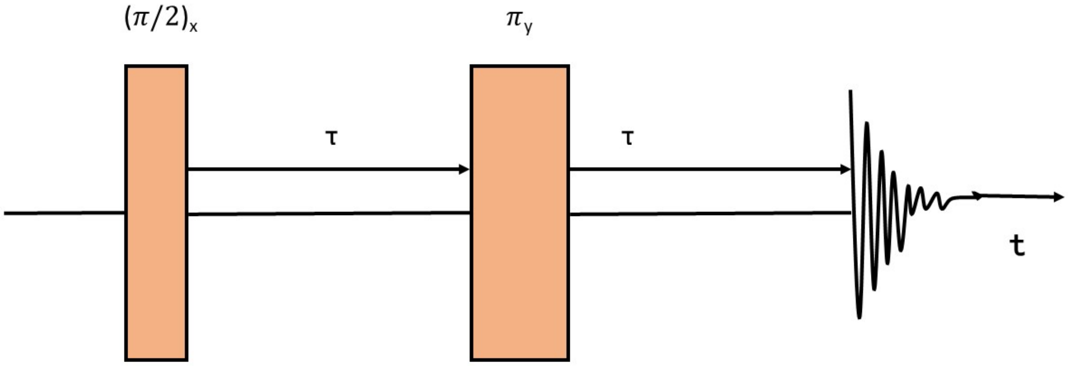

Figure (2.2) Spin echo pulse sequence [57]

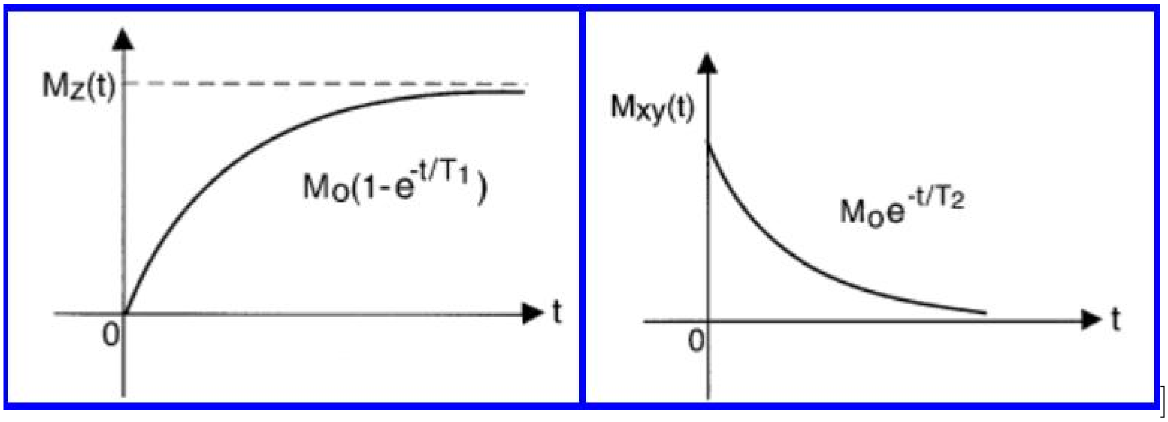

Figure (2.3) Growth of the magnetization vector in T_1 relaxation measurement (left) and decay in T_2 relaxation measurement(right). The transverse relaxation rate reported in this thesis is $R_2 = \frac{1}{T_2}$.

time, τ_c, is the time a molecule takes to rotate by 1 radian. The associated relaxation rates, $R_2 \equiv 1/T_2$, are related to the rotational correlation time through the Solomon equation,

$$R_2 \approx 3J(0) + 5J(\omega) + 2J(2\omega), \tag{2.6}$$

where $J(\omega)$ is the spectral density,

$$J(\omega) = \frac{\tau_c}{1 + (\omega\tau_c)^2}. \tag{2.7}$$

The higher the relaxation rates, the higher the constraint on the rotational motions of the molecule [58].

2.2.2 The Pulse-Acquire and Spin-Echo NMR experiments

We now discuss the simplest NMR experiments more formally. When a sample with NMR active nuclei is placed in an external magnetic field, their spins will be in a superposition state, with the wave function, $|\psi\rangle$,

$$|\psi\rangle = c_\alpha|\alpha\rangle + c_\beta|\beta\rangle. \tag{2.8}$$

$|c_\alpha|^2$ and $|c_\beta|^2$ gives the probability of the states $|\alpha\rangle$ and $|\beta\rangle$ respectively. If the population of $|\alpha\rangle$ is n_α, proportional to $|c_\alpha|^2$ and $\beta\rangle$ is n_β, which is proportional to $|c_\beta|^2$, then the net magnetization is related to the population difference by

$$M_z = \frac{1}{2}\gamma(n_\alpha - n_\beta). \tag{2.9}$$

On application of an RF pulse along the x-axis, the x-component of average magnetization is not affected, however, the y and z-component evolves as,

$$\langle I_y\rangle(t) = \langle I_y\rangle(0)\cos(\omega t) - \langle I_z\rangle(0)\sin(\omega t) \tag{2.10}$$

$$\langle I_z\rangle(t) = \langle I_z\rangle(0)\cos(\omega t) + \langle I_y\rangle(0)\sin(\omega t). \tag{2.11}$$

The magnetization vector is

$$M_i = \gamma N\langle I_i\rangle \tag{2.12}$$

where $i = x, y, z$. Initially the magnetization is only along z with a magnitude M_0 and zero on other two axis. The effect of RF pulse on the components of magnetization computed using equation 2.10, 2.11 and 2.12 are,

$$M_x(t) = 0 \tag{2.13}$$

$$M_y(t) = -M_0\sin(\omega t) \tag{2.14}$$

$$M_z(t) = M_0\cos(\omega t) \tag{2.15}$$

Therefore, if we apply an RF pulse for a duration t along x-axis such that the product of ω and t is $\frac{\pi}{2}$, the bulk magnetization will tilt to -y-axis, consistent with the prediction of right hand rule of vector analysis.

The density operator, defined as the outer product of the spin wave function and its conjugate wave, $\rho = \left|\psi\right\rangle\left\langle\psi\right|$ evolves as a function of time after the removal of the RF pulse. In a pulse acquire experiment, a $\left\langle\frac{\pi}{2}\right\rangle_x$ RF pulse is applied followed by a free evolution. During the $\left\langle\frac{\pi}{2}\right\rangle_x$ RF pulse, the density operator then evolves as

$$\widehat{\rho(t)} = \exp(-i\widehat{H}t)\rho(0)\exp(i\widehat{H}t) \tag{2.16}$$

where the Hamiltonian

$$\widehat{H} = \omega I_x, \tag{2.17}$$

and the density operator at t = 0 is $\widehat{\rho(0)} = \widehat{I_z}$. Using trigonometric identities and simple mathematical procedures, we can show,

$$\widehat{\rho(t)} = \cos(\omega t)\ \hat{I_z} - \sin(\omega t)\ \hat{I_y}. \tag{2.18}$$

If the frequency is applied for a duration such that the $\omega t = \frac{\pi}{2}$, then the magnetization will completely flip to the $-y$-axis, i.e, $\widehat{\rho(t)} = \widehat{-I_y}$. In a pulse acquire experiment, after the pulse, the magnetization undergoes a free evolution in the static magnetic field, for which the Hamiltonian is given by $H = \Omega I_z$

$$\Omega I_z\widehat{\rho(t)} = -\cos\Omega t\ \hat{I_y} + \sin\Omega t\ \hat{I_x}$$

which is the component being detected in a pulse-acquire experiment.

The spin echo experiment discussed in the previous section is a pulse-acquire experiment with an added π pulse applied (eg. along x) after a time τ. A spin echo will be observed exactly at a time τ after the π_x pulse. The result of the π pulse on the free evolution vector after the first $(\frac{\pi}{2})$ pulse is, $\cos\Omega\tau\hat{I}_y + \sin(\Omega\tau)\hat{I}_x$. Now, the free evolution of the vector with Hamiltonian $\Omega\hat{I}_z$ on the state after the π pulse is,

$$\Omega\hat{I}_z[\cos(\Omega\tau)\hat{I}_y + \sin(\Omega\tau)\hat{I}_x] = \cos(\Omega\tau)\cos(\Omega\tau)\hat{I}_y + \sin(\Omega\tau)\sin(\Omega\tau)\hat{I}_y = \hat{I}_y$$

Thus, there is a complete recovery of the signal at time τ after the π pulse. This is the spin echo.

2.2.3 The pulsed gradient spin echo (PGSE)

To study the translational motion of molecules, we perform the pulsed field gradient spin echo (PGSE) NMR experiment. In addition to the external magnetic field B, if there is a gradient in the magnetic field, $g = \frac{dB}{dz}$, the spins become spatially labelled with different Larmor precession frequency,

$$\omega = \gamma B + \gamma g z. \tag{2.19}$$

In PGSE, the pulse sequence remains the same as spin echo sequence. However, two gradient pulses of duration δ are applied at a time interval of Δ as shown in Figure 2.4. The first gradient induces a phase development in the spin precession and the second gradient inverts the developed phase. Therefore, in principle, if there are no molecular motions, a complete spin echo will be observed as in the SE experiment. If, the molecule has moved, the spin echo will be incomplete. Mathematically, the phase

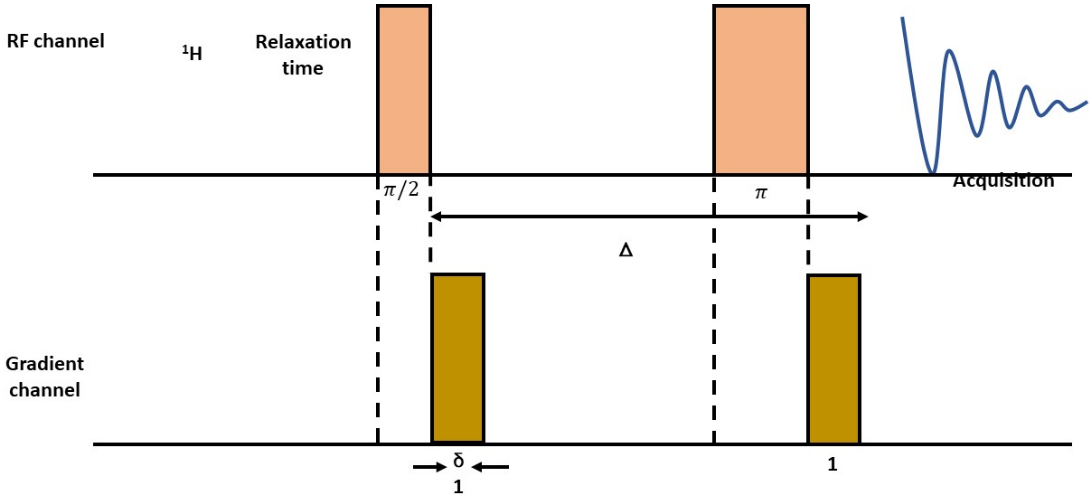

Figure (2.4) Pulsed field gradient spin echo NMR pulse sequence [59]

developed at the end of the first gradient is,

$$\phi(t) = \gamma B t + \gamma g \int_{t}^{t+\delta} z(t')dt', \tag{2.20}$$

after the second gradient,

$$\phi_{final} = \gamma g \left[\int_{t}^{t+\delta} z(t')dt' - \int_{t+\Delta}^{t+\Delta+\delta} z(t'')dt'' \right] \tag{2.21}$$

at time $t = 2\tau = \Delta$, the spin echo intensity is,

$$I\big(g, \delta, \Delta\big) = I_0 \int_{-\infty}^{\infty} P\big(\phi_{final}\big) \exp\big(i\phi\big) d\phi. \tag{2.22}$$

Upon ensemble averaging, assuming a Gaussian probability distribution for the phase accumulation, the complex exponential becomes a real, decaying exponential. When $\delta \ll \Delta$ and the gradient pulse is a rectangular pulse, the signal attenuation is given by [60],

$$I(g) = I_0 \exp\Bigg(-\gamma^2 g^2 \delta^2 D \Big(\Delta - \frac{\delta}{3}\Big)\Bigg)\Bigg(\exp\Big(\frac{-\Delta}{T_2}\Big)\Bigg) \tag{2.23}$$

However, if the transverse relaxation is much smaller than the longitudinal relaxation, then it imposes a restriction on the Δ. In such a case, a pulsed field gradient stimulated echo pulse is used to obtain the echo signal decay, discussed next.

2.2.4 The pulsed field gradient stimulated echo (PGSTE)

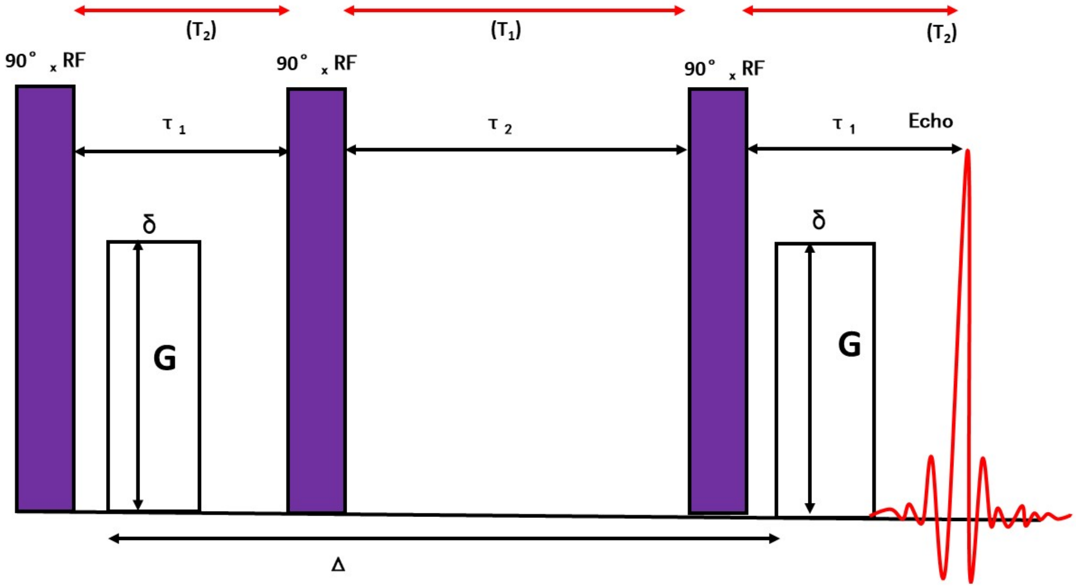

Figure (2.5) Pulsed field gradient stimulated echo NMR pulse sequence

In the pulsed field gradient stimulated echo pulse sequence (PGSTE), the second π pulse in SE is replaced by two $\frac{\pi}{2}$ pulses as shown in Figure 2.5. The second and third RF pulses can either both be along x or y. The RF pulses are shown in purple while the gradient pulses are the unfilled square pulses. The time duration between the second and third pulse (τ_2) is much longer than the duration between the first two pulses (τ_1). During time τ_2, the magnetization is "*stored*" along -z. A spoiler gradient is applied between the second and third RF pulse to destroy any transverse magnetization remaining. In systems with T_1 longer than T_2, for instance, the Ficoll suspensions studied here, the PGSTE is the better pulse sequence to study their diffusivity.

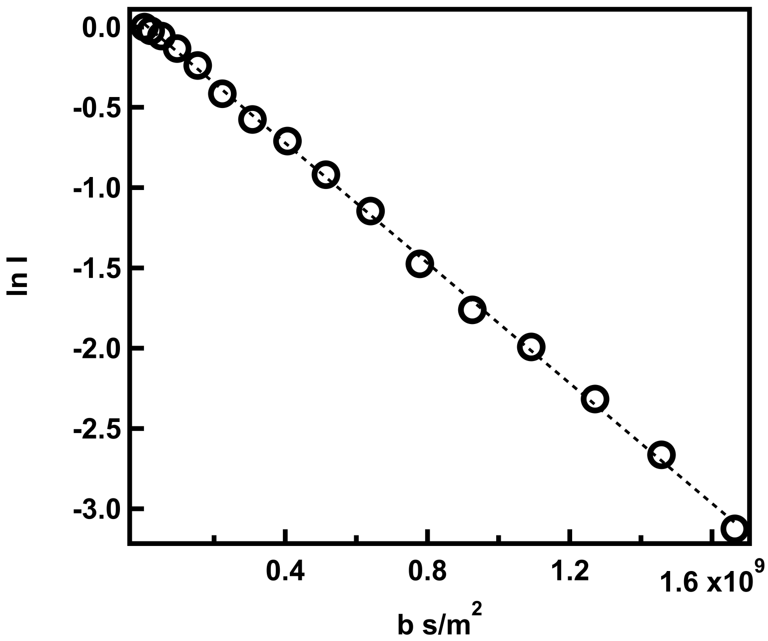

Figure (2.6) The natural logarithm of signal intensity vs gradient parameter $b = \gamma^2\delta^2 g^2(\Delta - \frac{\delta}{3})$ for D_2O, obtained using the PFG-STE pulse sequence. The slope yields the diffusion coefficient of trace HDO in D_2O and is used as a calibration standard $D = 1.902 \times 10^{-9}\ m^2$/s for all experiments.

To obtain the diffusion coefficient in a PGSTE experiment, the natural logarithm of the signal intensity is plotted against the gradient intensity parameter, b, given by

$$b = \left(\gamma g \delta\right)^2 \left[\Delta - \frac{\delta}{3}\right] \tag{2.24}$$

where $\gamma = 2.675 \times 10^8/sT$ is the gyromagnetic ratio of the hydrogen nucleus, g is the applied magnetic field gradient (applied as a nearly square trapezoidal pulse of duration $\delta = 2\ ms$, and $\Delta = 50\ ms$ is the diffusion time). For single component species, the intensity decay would be mono-exponential, with the form

$$I(b) = I(0) * \exp((-bD) \tag{2.25}$$

The slope of a plot of $\ln(I(b))$ vs b gives the diffusion coefficient D of the molecule. The intensity decay for D_2O obtained using the PGSTE pulse sequence is shown in shown in Figure 2.6. The diffusion coefficient of trace HDO in D_2O is used as a calibration standard $D = 1.902 \times 10^{-9}$ m^2/s for all experiments.

2.2.5 Double stimulated echo pulse sequence

Any directed flow on top of the Brownian motion of the suspensions can give rise to artifacts in the diffusion measurement. Such flow could arise due to events such as thermal convection due to a temperature gradient in the sample. The presence of a thermal gradient can be detected by performing a diffusion for different diffusion time (Δ) in a pulsed field gradient stimulated echo, otherwise keeping the sample conditions identical. If thermal convection is present, it will manifest as an increase in the diffusion coefficient with increase in Δ [61, 62]. In a high magnetic-field-gradient instrument such as the one in our laboratory (1800 G/cm), the possibility of eddy currents on applying the field gradients is not negligible and can cause error in baseline and phase in the spectra [63]. Bipolar gradients are used to compensate for eddy currents. To suppress the effect of convection, a double stimulated echo pulse can be used as shown in Figure 2.7. In a double stimulated echo sequence, the diffusion time Δ is split into such that each half of the cycle resembles the basic STE. The unwanted convection generated echos arising from the first STE will be cancelled by the echos from the second STE [62].

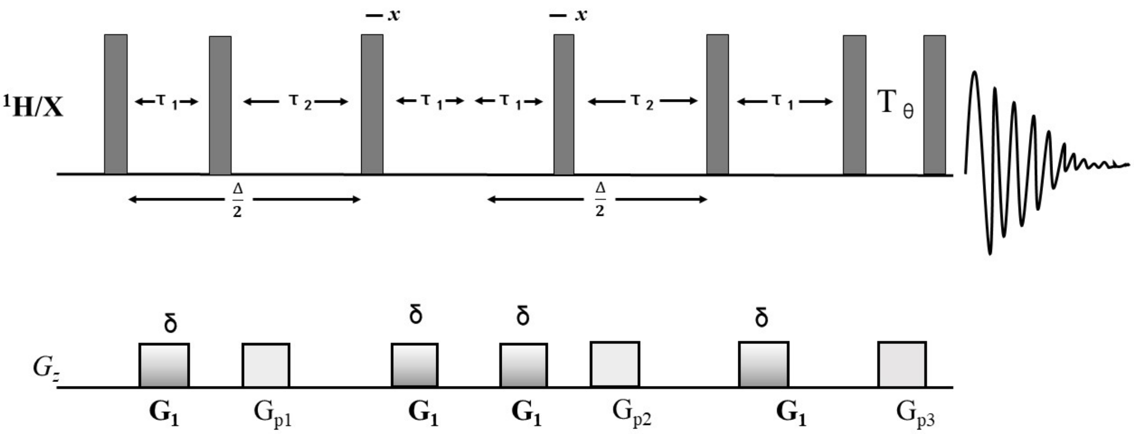

Figure (2.7) Double stimulated echo pulse sequence

2.2.6 Convection compensation: Alternative approach

For a thermal gradient to set up convective flow in a cylindrical tube of radius r, the Rayleigh number, Ra, is given by

$$Ra = \frac{g\alpha}{k\nu'} r^4 T^\star \tag{2.26}$$

where g is the acceleration due to gravity, α is the thermal expansivity, k is the thermal diffusivity, ν' is the kinematic viscosity and $T^\star$ is the thermal gradient [62]. In our experiments, reducing the inner radius of the tube, is therefore, a very effective way to suppress the convection. For all our experiments, we employ a home made NMR insert tube (with an inner diameter of 4mm) which is inserted to a 5 mm NMR tube.

2.2.7 Coherence transfer path ways and phase cycling

In this section, we discuss coherence transfer pathways briefly. When an ensemble of nuclear magnetic resonance active nuclei are placed in an external magnetic field, some of the magnetic moments align parallel to the magnetic field and some align anti parallel. When tilted at an angle β, the magnetic moments precess at Larmor frequency in phase and are said to be coherent. Their coherent precession is mathematically represented by [56],

$$\hat{R} = \hat{R}\exp(-ip\phi) \tag{2.27}$$

$\hat{R}$ is the rotational operator which rotates the vector from z-axis about an angle ϕ. p is the coherence order. $p = 0$ is the z magnetization. If an operation result in $p = \pm 1$, then its said to be in single quantum coherence, $p = \pm 2$ for double quantum coherence and so on. In an operation where the magnetization is rotated to -y-axis by applying an RF pulse in the x-axis, it generates all the coherence orders allowed for single quantum coherence. Mathematically,

$$\hat{I_x} = \frac{1}{2}\left[\hat{I_+} + \hat{I_-}\right] \tag{2.28}$$

The operator $\hat{I_+}$ has a coherence order of +1 and $\hat{I_-}$ has a coherence order of -1. In the modern NMR spectrometer, only the signal with coherence order, p=-1, is designed to be detected [56]. Phase cycling is an approach to eliminate any unwanted signals with coherence order that are not equal to -1. Figure 2.8 shows the possible single quantum coherence pathways. In the three generated coherences, the only desired signal corresponds to p=-1. To achieve this, we adjust the phase of the receiver,

$$\phi_{receiver} = -\Sigma_{m=1}^{m=n}\Delta p\phi_m \tag{2.29}$$

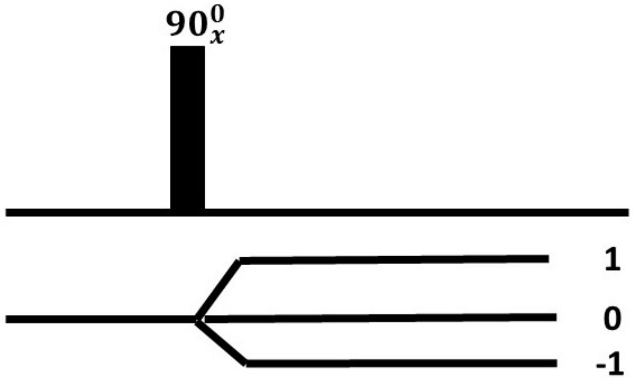

]

Figure (2.8) Coherence path ways for a single 90_x^0 pulse.

where m is the number of pulses and ϕ_m is the pulse phase in the sequence. The phase of the pulse is $\frac{2\pi}{\Delta k}$ where $\Delta k = \Delta p_{max}$ - Δp_{min} + 1. In the case of single pulse sequence, $\Delta p_{max} = 1$ and $\Delta p_{min} =$ -1 leading to $\Delta k = 3$. The pulse phase, therefore, has to be advanced in steps of $\frac{2\pi}{3}$. For m pulses, there will be 3^m coherence order generated. To pick the signal with coherence order -1 for single pulse, for full phase cycle we need three scans with phases 0, $\frac{2\pi}{3}$ and $\frac{4\pi}{3}$.

2.3 Small Angle Neutron Scattering (SANS)

The pioneering work by Guinier introduced the concept of small angle scattering in the 1930's [64]. He used small angle X ray scattering to study metal alloys. In the 1960's, neutron research started developing to use neutrons for performing small angle neutron scattering (SANS) experiments [65]. SANS is now recognized as a powerful technique to address many experimentally challenging questions. The method of deuterating only the polymer chains of interest, in a protonated surrounding helps to enhance the contrast in neutron scattering experiments. Understanding the structure at segmental length scale, therefore, becomes possible with the help of SANS [66]. In 1974, Heinrich *et al.* studied H-D exchange reaction in proteins, obtained the molecular weight distribution and the radius of gyration of biological macromolecules [67]. They concluded that SANS is a superior technique over other techniques like small angle X-ray scattering (SAXS) to study the H-D exchange in macromolecules apart from obtaining radius of gyration, shape and interaction in the system. Moreover, unlike X-rays, which can ionize the sample under study, neutrons are far weaker interacting. Neutrons neither ionize the sample nor heat it up. Therefore, SANS is a widely used experimental technique to study biological samples [65].

In the present work, we perform our SANS experiments at the National Institute of Standards and Technology (NIST), USA. At NIST, thermal neutrons are used for scattering experiments. Thermal neutrons are neutrons that correspond to an energy of 25 meV. Typically, a fission reaction produces energy of 200 MeV. The moderators, usually, heavy water, slow down the fast neutrons produced in the fission reaction. These thermal neutrons help in sustaining the fission reaction and are also used for scattering experiments [68]. Neutron guides transport these thermal neutrons to the guide hall. The 30m SANS instrument is installed on a split neutron guide, NGB-30. The scattering vector, q, which is the difference between incident and scattered wave vector, falls in the range of 0.0015 to 0.6 $Å^{-1}$ [69]. The corresponding probe size is between 10 to 4000 Å. The reactor operates at 20 MW, and is a liquid hydrogen moderated, helium gas refrigeration supported research reactor. A filter, consisting of Bismuth (Bi), filters the fast neutrons and absorbs the γ radiations produced from the source. A multidisk velocity selector is used to monochromatize the incident beam and also to control the spread of the wavelength [69]. The monochromatized beam is then collimated by circular apertures before it reaches the sample stage. A two-dimensional position sensitive neutron detector records the scattered neutrons from the sample.

Strictly following the NIST data reduction package [70], we obtain the one-dimensional intensity curve as a function of the scattering vector. We first obtain the transmission of the sample container. This will be subtracted to obtain sample transmission from the total transmitted neutron flux. The sample transmission is then normalized against the empty beam transmission to obtain absolute scaled intensity. We follow the NIST tutorials to reduce the absolute scaled intensity using Igor Pro software [71].

2.3.1 Theory

In a small angle neutron scattering experiment, we measure the ratio of scattered neutron intensity to the incident neutron intensity [72]. Suppose that a neutron flux of intensity I_0 hits the sample, and scatters to the two dimensional position detector, then

$$d\sigma = \frac{I_s r^2 d\Omega}{I_0} \tag{2.30}$$

where, $d\sigma$ is the differential cross section, $r^2 d\Omega$ is the scattering area in which r is the distance of the detector from the sample and $d\Omega$ is the solid angle. Under the static approximation, which assumes that the light mass neutrons do not displace the heavy mass molecules in the sample upon scattering and the energy transfer is negligibly small [72], the differential scattering cross section, is given by

$$\frac{d\sigma}{d\Omega} = \frac{1}{V}\left\langle \left| \sum_{l=1}^{N} b_l \exp(iq.r_l) \right|^2 \right\rangle \tag{2.31}$$

where b_l is the bound scattering length of the scattering nucleus and V is the total volume.

Consider a colloidal sample which subdivides to N cells, and each cell has a colloidal particle at its center. Assume that the position vector of the j^{th} nucleus at the i^{th} cell has a position vector of the center of mass R_i and position vector relative to the center of mass X_i, then the differential scattering cross section can be written as

$$\frac{d\sigma}{d\Omega} = \frac{1}{V}\left\langle \left| \sum_{i=1}^{N} \exp(iq.R_i) \sum_{cellj} b_{ij} \exp(iq.X_j) \right|^2 \right\rangle \tag{2.32}$$

the quantity $\sum_{cellj} b_{ij} \exp(iq.X_j)^2$ is the form factor of the colloidal suspension. For a mono-disperse colloidal particle suspension, the form factor is identical for each particle and the differential scattering cross section is given by,

$$\frac{d\sigma}{d\Omega} = \frac{N}{V}|F(q)|^2 \frac{1}{N}\left\langle \sum_{i=1}^{N}\sum_{j=1}^{N} \exp(iq.(R_i - R_j)) \right\rangle. \tag{2.33}$$

In the above expression, $|F(q)|^2$ is the particle structure factor $P(q)$. The structure factor $S(q)$ is

$$S(q) = \frac{1}{N}\left\langle \sum_{i=1}^{N}\sum_{j=1}^{N} \exp(iq.(R_i - R_j)) \right\rangle. \tag{2.34}$$

The differential scattering cross section thus can be written as,

$$\frac{d\sigma}{d\Omega} = \frac{N}{V}P(q)S(q). \tag{2.35}$$

The form factor analysis leads to the estimation of the volume of the object, radius of gyration of the particle and fractal dimension [73]. If the volume fraction of the colloidal suspension is ϕ then, the scattered intensity as q goes to zero is,

$$\lim_{q \to 0} I(q) \propto \phi v_{object} \tag{2.36}$$

where v_{object} is the volume of the object. Regardless the shape of the particle, its volume can be calculated as above. For an isotropic system that is free to rotate in all directions, the form factor is,

$$P(q) = \frac{1}{N^2} \sum_{i=1}^{N} \sum_{j=1}^{N} \frac{\sin(qr_{ij})}{qr_{ij}} \tag{2.37}$$

In the low q regime, SANS probes spatial scales much larger than the object. Then for qr_{ij} less than 1, expanding the sinusoidal term and neglecting the higher orders, the form factor will be,

$$P(q) = 1 - \frac{q^2}{3} \left[\frac{1}{2N^2} \sum_{i=1}^{N} \sum_{j=1}^{N} r_{ij}^2 \right] = 1 - \frac{q^2 {R_g}^2}{3} \tag{2.38}$$

where R_g is the radius of gyration. This is known as the Guinier approximation.

2.3.2 Form factor and structure factor

The form factor, $P(q)$, of a scattering object is the scattering intensity of the suspensions in dilute solution. The scattering intensity at any higher concentration will be the product of the form factor, $P(q)$, and the structure factor $S(q)$. Provided that the form factor is independent of the sample concentration, the ratio of scattering intensity at any concetration to the form factor will give the structure factor of the suspensions.

$$S(q) = \frac{I(q)}{P(q)} = \frac{P(q)S(q)}{P(q)} \tag{2.39}$$

In systems composed of soft particles or polymers, however, $P(q)$ may not be independent of concentration, equation 2.39 must be used with care.

2.3.3 Rheology

We examine the variation of viscosity of the colloidal suspensions using Anton-Paar MCR 301 rheometer. On application of a shear force on a sample confined under the given space, the upper layer of the suspension undergoes a displacement while the bottom layer remains stationary creating a shear profile as shown in Figure 2.9. The shear stress then is defined as $\sigma = \frac{F}{A}$ and the shear strain γ is given by $\frac{x}{h}$ and the shear rate is $\dot{\gamma} = \frac{d\gamma}{dt}$. For a Newtonian suspension, the shear stress is proportional to shear rate and the proportionality constant is called the dynamic viscosity, η, a measure of sample resistance to flow against the applied force. In this thesis, we employ a cone and plate geometry of angle 0.5^o with truncation distance 0.053 mm to shear the suspensions. The shear rate was varied from 10-200 $1/s$ and the shear stress development is monitored. The cone and plate geometry assures uniform shear across the sample. We prepare the Ficoll suspensions in 0.2 % sodium dodecylsulphate, a surfactant. This small amount of surfactant does not affect the viscous properties of the suspension, but reduces the interfacial tension artefact, especially at low Ficoll concentrations and low shear rates. All the data were taken at a temperature of 25^o Celsius.

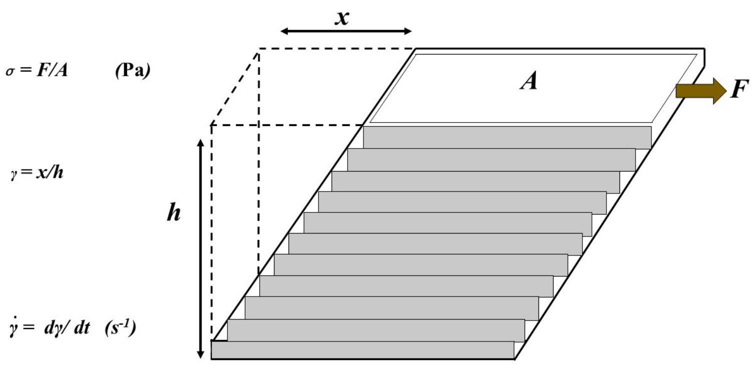

Figure (2.9) Shear profile of sample under the action of external shear force.

Chapter 3

Is Ficoll a colloid or polymer? A multi-technique study of a prototypical excluded-volume macromolecular crowder

3.1 Introduction

It is accepted that the in-cell environment is a crowded, macromolecular soup with a variety of macromolecules, at high total concentrations (300 - 400 g/l), occupying a significant fraction of the total volume [74]. This excluded volume is a primary input to any fundamental understanding of macromolecular crowding [75]. An elucidation of the relative importance of excluded volume and other non-specific interactions [76] is predicated on a knowledge of the volume occupied by macromolecules as a function of concentration. Yet even for the simplest macromolecular crowder, Ficoll (a branched and internally crosslinked polysucrose that is a co-polymer of sucrose and epichlorohydrin), the analogy with a hard-sphere-colloid crowder is only approximate [77, 78]: indeed various studies have proposed that Ficoll could be a semi-rigid sphere [79, 44], an elongated spherocylinder or rod [80, 81], an open deformable structure [82, 83], a porous particle [84] or a particle with multiple diffusive modes [85].

A colloidal model or a rigid-particle-based picture, however, has been found to be only partly adequate in diverse polymer and protein systems. Two examples are crosslinked microgels, whose polymer-colloid duality is now well recognized [86], and globular proteins, where a purely colloidal picture is not adequate to capture protein solution properties [50, 87].

In this work, we employ multiple experimental techniques to evaluate the structure and hydration properties of Ficoll suspensions. We obtain complementary views of Ficoll from the points of view of non-equilibrium response (rheology), quiescent equilibrium structure (SANS), and equilibrium Brownian diffusion and relaxation (NMR) dynamics. Under steady shear, the Ficoll viscosities exhibit a concentration dependence that is completely consistent with a crossover between dilute linear chains and reptating polymer chains exhibiting $c^{15/4}$ (de Gennes) scaling [88]. Our neutron scattering experiments, in addition, conclusively indicate that the low-concentration structure of Ficoll is consistent with that of a linear Gaussian polymer. Employing complementary NMR methods, we demonstrate, for the first time, that two different Ficolls, Ficoll-70 and Ficoll-400 are super-hydrated and occupy a volume that increases in a nonlinear fashion with the mass concentration. This volume fraction greatly exceeds the value assumed in numerous previous studies (including our own [28, 84]) that have assumed a Ficoll volume of $\bar{v}(ml/g) \times m(g)$ where $\bar{v}$ corresponds to the specific volume of Ficoll and has a value of $0.65 - 0.67$ ml/g [89, 84] for Ficoll-70 and 0.68

ml/g [89, 90] for Ficoll-400. This result *would affect all past studies* that compare crowding using Ficoll to models of rigid crowder particles of any shape.

3.2 Materials and methods

3.2.1 Sample preparation

Ficoll-400 and Ficoll-70 (with molecular weights of 400 kDa and 70 kDa respectively) were purchased from Sigma-Aldrich. In each experiment, the required amount of Ficoll, m_F is first weighed and then dispersed in D_2O of mass m_{D_2O} using a Fisherbrand homogenizer. The sample is stirred using a 7mm homogenizer probe for 3 minutes at 11000 rpm. This procedure is repeated 5 times with an interval of 1 minute between each stirring. The weight fraction of the suspensions is

$$c_{\mathrm{F}} = \left[\frac{m_F}{m_F + m_{D_2O}}\right] \times 100, \tag{3.1}$$

as a concentration in wt %, or in w/w as a fraction between 0 and 1.

3.2.2 Nuclear magnetic resonance diffusion and relaxation

The samples for NMR measurements were filled in a capillary tube that fits into a 5mm NMR tube to remove the effects of convection (see Section 2.2.6). Experiments were conducted at 298 K using a Bruker Avance II NMR spectrometer at a ^1H resonant frequency of 600 MHz. Details of diffusion and nuclear magnetic relaxation experimental probe parameters and methods are described in the Appendix.

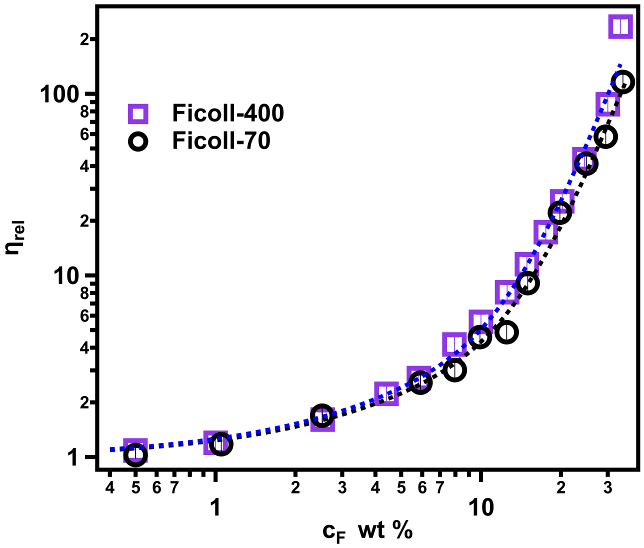

(a)

Figure (3.1) **Rheology:** The relative viscosity, for both Ficoll-70 and Ficoll-400 suspensions, follows polymer scaling with a crossover from dilute to semi-dilute behaviour. The dotted lines are fits to equation 3.2.

3.2.3 Small Angle Neutron Scattering

The small angle neutron scattering (SANS) experiments were performed on the NGB-30m beam line at the Center for Neutron Research at the National Institute of Standards and Technology [69]. We reduced the 2-D neutron scattering intensity by following the methods outlined by Klein and co-workers, [70]. Details of the reduction of neutron scattering intensity is provided in the Appendix.

3.3 Results and Discussion

3.3.1 Rheology: Polymer-like behaviour of Ficolls

We begin by evaluating the sample bulk properties of the Ficoll suspensions by steady-shear experiments in a cone-plate rheometer probed between shear rates $\dot{\gamma}$ from 10 -

200 1/s. At all concentrations, the response is Newtonian, but the viscosities depend in a nonlinear fashion on the concentration shown in Figure 3.1. We fit the relative viscosity ($\eta_{\text{rel}} \equiv \eta_{\text{suspension}}/\eta_{\text{solvent}}$) of the Ficoll suspensions to the form

$$\eta_{\text{rel}} = 1 + \left[c_{\text{F}}[\eta]_0 + k_{\text{H}}(c_{\text{F}}[\eta]_0)^x \right], \tag{3.2}$$

where $[\eta]_0$ is associated with the intrinsic viscosity, and in our formulation is dimensionless (since c_{F} is a mass fraction). Equation 3.2 was employed by Tuinier et al [14] for a natural polysaccharide with a single backbone, the functional form captures the crossover from dilute solution behaviour where $\eta_{\text{rel}} \propto c_{\text{F}}$ to the concentrated de Gennes reptation regime where $\eta_{\text{rel}} \propto c_{\text{F}}^{15/4}$ [88]. We obtain $[\eta]_0 = 0.234 \pm 0.003$ for Ficoll-70 and 0.261 ± 0.003 for Ficoll-400. We also obtain an exponent $x = 3.87 \pm 0.11$ for Ficoll-70 and 3.71 ± 0.09 for Ficoll-400, which is remarkably consistent with the de Gennes value 15/4 [88]. The prefactor k_{H}, identified as the Huggins constant, is a measure of hydrodynamic interactions between macromolecules: we obtain $k_{\text{H}} = \frac{1}{25}$, numerically the same as obtained for the natural polysaccharides [14]. This result, indicating polymer-like behaviour, encourages us to look beyond the hard-sphere paradigm.

3.3.2 SANS: The form factor of Ficoll-400

For soft, deformable particles, it can be the case that the apparent structure under shear is not the same as the structure in the quiescent state. We used SANS to extract the structure of Ficoll, in dilute solution, in the quiescent state. Given the reasonable assumption of the absence of particle-particle interactions in the most dilute solution probed ($c_{\text{F}} = 1\%\frac{w}{w}$), we consider this to be the form factor. We report the normalized neutron scattering intensity of Ficoll-400 (details of SANS methods in Appendix),

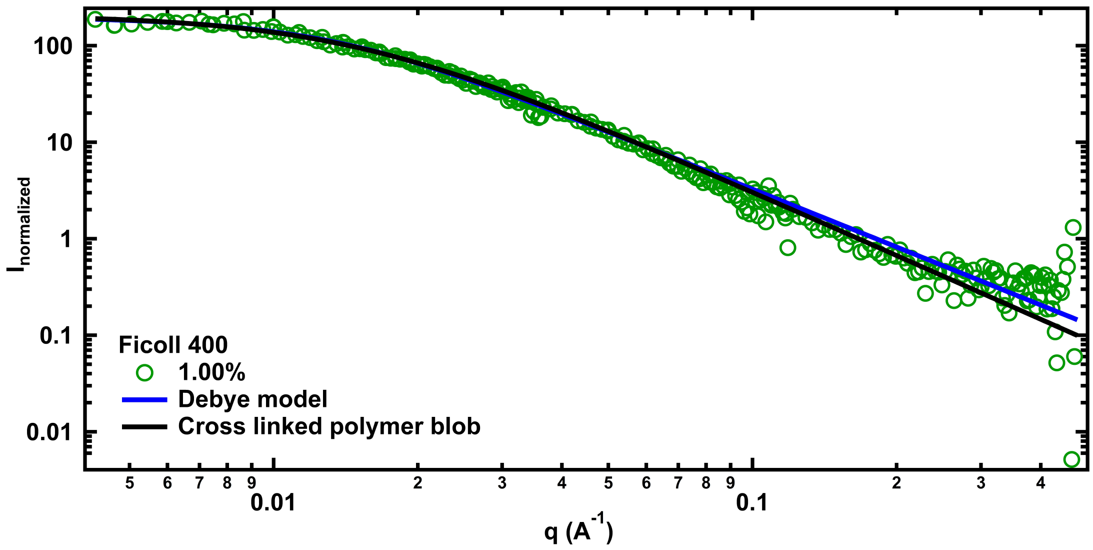

(a)

Figure (3.2) **SANS form factor:** Form factor of Ficoll-400 obtained at the lowest concentration, $c_{\mathrm{F}} = 1\%\frac{w}{w}$ as a function of the scattering vector q. A good fit is achieved to both the Debye model (for a linear Guassian polymer) and an extended Debye–Anderson–Brumberger model for a crosslinked polymer blob.

which, because of its larger size, is a better neutron scatterer than Ficoll-70 at 1% $\frac{w}{w}$. This is depicted in Figure 3.2.

Interestingly, we do not observe any hint of Bessel-like oscillations in the form factor, a typical characteristic of hard sphere colloids [91]. Rather, the form factor (the scattered intensity $I(q)$ at the lowest concentration) is a smoothly decreasing function of q, and is well fit by the Debye model for Gaussian polymer chain, with a form factor

$$P(q) = \frac{I(q)}{I_0} = \left(\frac{2}{y^2}\right)\Bigg[\exp(-y) + y - 1\Bigg], \tag{3.3}$$

where y = $q^2R_g^2$, and R_g is the radius of gyration. From the fit (blue curve in Figure 3.2), we obtain an R_g of 11.07 ± 0.08 nm. We know that the Ficolls are highly-branched and crosslinked. Thus, we also tried to fit the experimental form factor to a polymer blob model [92]. The fit to the data is equally good (black curve in

Figure 3.2), but requires an additional free parameter. The R_g obtained from the Debye fit is also consistent with the model-independent R_g obtained from the Guinier regime. We obtain a size ratio $\frac{R_{\mathrm{g}}^{\mathrm{SANS}}}{R_{\mathrm{H}}^{NMR}} = 1.52 \pm 0.03$ using the radius of gyration, obtained by fitting the Debye model to the SANS form factor, and the hydrodynamic radius, obtained from Ficoll-400 diffusivity measurements in dilute solutions (NMR experiments, discussed next). The theoretical value for the universal size ratio for a linear Gaussian polymer is 1.5045 [93] while a value of 1.59 ± 0.01 is predicted by Dunweg *et al* for polymer chains in good solvent, who comment that the true error is likely larger than the value they quote. In short, an experimental value of $\frac{R_{\mathrm{g}}^{\mathrm{SANS}}}{R_{\mathrm{H}}^{NMR}}$ between 1.5 and 1.6 is consistent with predictions using slightly different simulation models. Thus, we conclude that the Ficoll molecules have distinct polymer-like properties. Next, we examine the nature of the free volume accessible for other molecules in Ficoll suspensions of different concentrations using different NMR methods.

3.3.3 NMR: concentration dependent volume fraction of Ficoll

Different species can be distinguished in NMR spectroscopy *via* the chemical shift. Thermally driven Brownian motion and rotational motions affect measurable quantities, i.e., diffusion and relaxation in multi-component macromolecular solutions [94], and can be obtained for both the water (in the present case, trace HDO molecules in the D_2O) and the Ficoll.

Diffusion: The self-diffusion coefficients of HDO molecules in Ficoll-D_2O solution are plotted as a function of Ficoll concentration, c_{F}, for both Ficoll-70 and Ficoll-400 in Figure 3.3(a). They are obtained from signal attenuations that are mono-exponential at all c_{F} (Appendix Figure A1(b)). As a function of c_{F}, the diffusion coefficient D^{HDO}

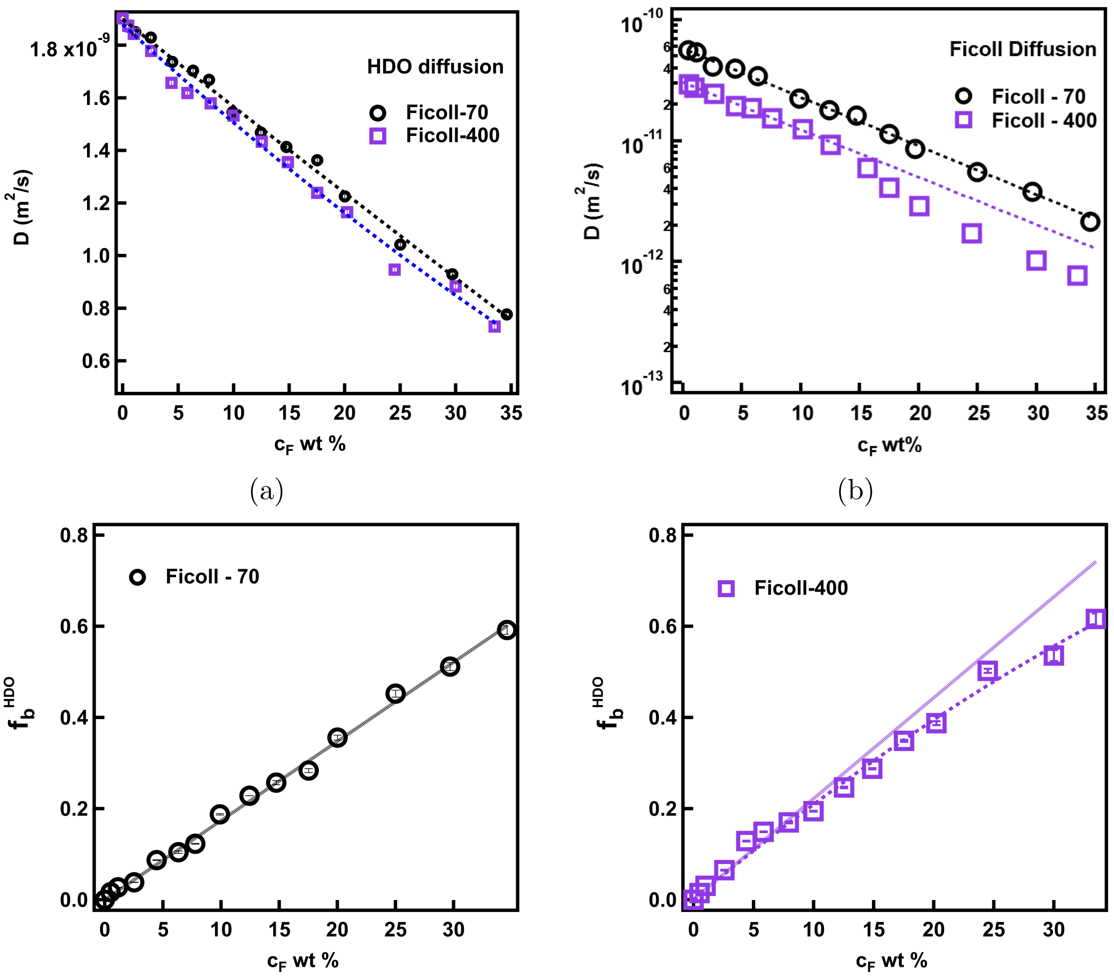

(a) (b)

(c) (d)

Figure (3.3) **PFG-NMR:** (a) Self diffusion coefficient of trace HDO in Ficoll-D_2O solution decreases linearly with increase in Ficoll weight fraction, c_{F} with a small quadratic dependence at high concentrations for both Ficoll-70 and Ficoll-400. (b) Self diffusion coefficient of Ficoll-70 and Ficoll-400 exhibits a much more dramatic (exponential) decrease as a function of c_{F}. (c) Ficoll-bound water fraction f_b^{HDO} (Equation 3.5) increases linearly for Ficoll-70. (d) f_b^{HDO} increases linearly until 10 % $\frac{w}{w}$ for Ficoll-400 and has a quadratic contribution when fit over the entire concentration range.

decreases. The decrease is roughly linear, with a small quadratic correction at higher concentrations, $D^{\mathrm{HDO}} = D_0^{\mathrm{HDO}}(1 - k_1 c_{\mathrm{F}} - k_2 c_{\mathrm{F}}^2)$. For Ficoll-70 and Ficoll-400, we obtain $D_0^{\mathrm{HDO}} = (1.89 \pm 0.01) \times 10^{-9} m^2/s$ and $(1.88 \pm 0.02) \times 10^{-9} m^2/s$ respectively, consistent with the bulk HDO-in-D_2O calibration value [95] of $1.902 \times 10^{-9} m^2/s$.

At the highest concentrations, the reduction in D^{HDO} is significant, i.e., 60% lower than the bulk value. Models of "obstructed diffusion" have been employed in the past [96, 97], which show a more more modest (25%) reduction in $D^{\mathrm{HDO}}/D_0^{\mathrm{HDO}}$. Given that we know, first, that there is significant water in the Ficolls, and second, that there will be very rapid exchange between free and bound water molecules, we expect a single observable diffusion mode for the water (i.e., mono-exponential dependence on the gradient parameter b of the raw signal attenuation), which is what we observe (Appendix Figure A1(b)), with an observed diffusion coefficient

$$D^{\mathrm{HDO}}(c_{\mathrm{F}}) = f^{\mathrm{HDO}} D^{\mathrm{HDO}}(0) + (1 - f^{\mathrm{HDO}}) D_{\mathrm{bound}}^{\mathrm{HDO}} \tag{3.4}$$

The self-diffusivity of the Ficoll particles is shown in Figure 3.3(b). Since the Ficoll diffusion shows two distinct modes (see Experimental Methods and Appendix Figure A1(a)) we plot the average Ficoll diffusion coefficient D_{ave} given by Equation A.2. D_{ave} shows an exponential decrease, with a fit giving characteristic concentrations of 10.76 ± 0.47 and 11.59 ± 0.68 wt % for Ficoll-70 and Ficoll-400. D_{ave} is approximately 2 orders of magnitude lower than D^{HDO} in the dilute limit, and 3 orders of magnitude lower at $c_{\mathrm{F}} = 15\%$. Since the Ficoll-bound water will diffuse as fast as the Ficoll itself, i.e., $D_{\mathrm{bound}}^{\mathrm{HDO}} \equiv D_{\mathrm{ave}}$, we can write an expression for the "bound" HDO fraction (which reflects on the total bound D_2O):

$$\begin{aligned} f_b^{\mathrm{HDO}} \equiv 1 - f^{\mathrm{HDO}} &= (1 - D^{\mathrm{HDO}}(c_{\mathrm{F}})/D^{\mathrm{HDO}}(0))/(1 - D_{\mathrm{ave}}(c_{\mathrm{F}})/D^{\mathrm{HDO}}(0)) \\ &\approx 1 - D^{\mathrm{HDO}}(c_{\mathrm{F}})/D^{\mathrm{HDO}}(0) \end{aligned} \tag{3.5}$$

where f^{HDO} is the fraction of bulk (i.e., free) HDO molecules and $f_b^{\mathrm{HDO}} \equiv 1 - f^{\mathrm{HDO}}$ is the fraction of Ficoll-bound HDO. Here, Ficoll-70 and Ficoll-400 show slightly different behaviours. While f_b^{HDO} increases linearly with c_{F} for Ficoll-70 (Figure 3.3 (c)), there is a nonlinearity at higher concentrations for Ficoll-400. Perhaps related, we also observe a small, but noticeable, deviation from the exponential decrease in the self diffusion coefficient of Ficoll-400 above $c_{\mathrm{F}} = 15\%$, while Ficoll-70 shows a simple exponential decrease.

We fit the concentration dependence of f_b^{HDO} to linear and quadratic contributions, $f_b^{\mathrm{HDO}} = k_1 c_{\mathrm{F}} + k_2 c_{\mathrm{F}}^2$: $k_1 = 0.0173 \pm 0.0001$ and the quadratic contribution is zero for Ficoll-70 (Figure 3.3 (c)) while for Ficoll-400, $k_1 = 0.022 \pm 0.001$ and the quadratic contribution is $k_2 = -1.18 \times 10^{-4} \pm 3.77 \times 10^{-5}$ small but non-zero and is in fact noticeable above 10 % $\frac{w}{w}$ (Figure 3.3 (d)).

Effective volume fraction: The finding that such a large fraction (up to 60%) of the water is associated strongly with the Ficolls implies that it is incorrect to obtain the pervaded Ficoll volume at all concentrations by multiplying the mass by a specific volume, i.e.,

$$\phi_s = \frac{\bar{v} m_F}{\bar{v} m_F + V_{\mathrm{D_2O}}}, \tag{3.6}$$

except in the dilute limit. The specific volume $\bar{v}$ has a value of 0.65 – 0.67 ml/g [89, 84] for Ficoll-70 and 0.68 ml/g [89, 90] for Ficoll-400. Indeed, a significant part of the hydrodynamic volume occupied by the Ficolls is water, and this water is not part of the free volume accessible to other macromolecules!

Thus we calculate an effective Ficoll volume, V_{eff} which includes the specific volume of the Ficoll *and* the volume of bound water, defined as

$$V_{\text{eff}} = \bar{v} m_F + {f_b}^{HDO} V_{D_2O}, \tag{3.7}$$

where $\bar{v}$ is the specific volume (0.65 ml/g for Ficoll-70 and 0.68 ml/g for Ficoll-400), m_F is the mass of the Ficoll molecule in the suspension, ${f_b}^{HDO}$ is the fraction of bound HDO molecules and V_{D_2O} is the volume of D_2O. Then the effective volume fraction is given by

$$\phi_{\text{eff}} = \frac{V_{\text{eff}}}{V_{\text{eff}} + (1 - {f_b}^{HDO} V_{D_2O})}. \tag{3.8}$$

Importantly, the solvent "free" volume is reduced by the volume of bound water that is part of the Ficoll effective volume.

Alternatively, we can also estimate the Ficoll volume fraction by estimating the hydrodynamic volume of the Ficoll molecules. For dilute systems, this volume would simply be $V_{\text{hydrodynamic}} = \left[\frac{4}{3}\pi R_h^3\right]\left[\frac{m_F}{M_w}\right] N_A$, where m_F is the mass of Ficoll, M_w is the molecular weight of Ficoll-400 (400kDa), and N_A is the Avogadro's number. The hydrodynamic radius can be obtained from the measured self-diffusion coefficients of Ficoll (Figure 3.3(b)) at the lowest concentrations (using the Stokes-Einstein equation) and has a value of 4.06 ± 0.08 for Ficoll-70 and 7.26 ± 0.11 for Ficoll-400. So long as $f_b^{\text{HDO}} \propto c_{\text{F}}$, the bound water per Ficoll particle is constant. A concentration dependent hydrodynamic volume must therefore account for the k_2-dependent nonlinear term in the relationship of f_b^{HDO} with c_{F} in Figure 3.3(c,d):

$$V_{\text{hydrodynamic}} = \left(1 + \frac{k_2}{k_1} c_{\text{F}}\right) \left[\frac{4}{3}\pi R_h^3\right] \left[\frac{m_F}{M_w}\right] N_A. \tag{3.9}$$

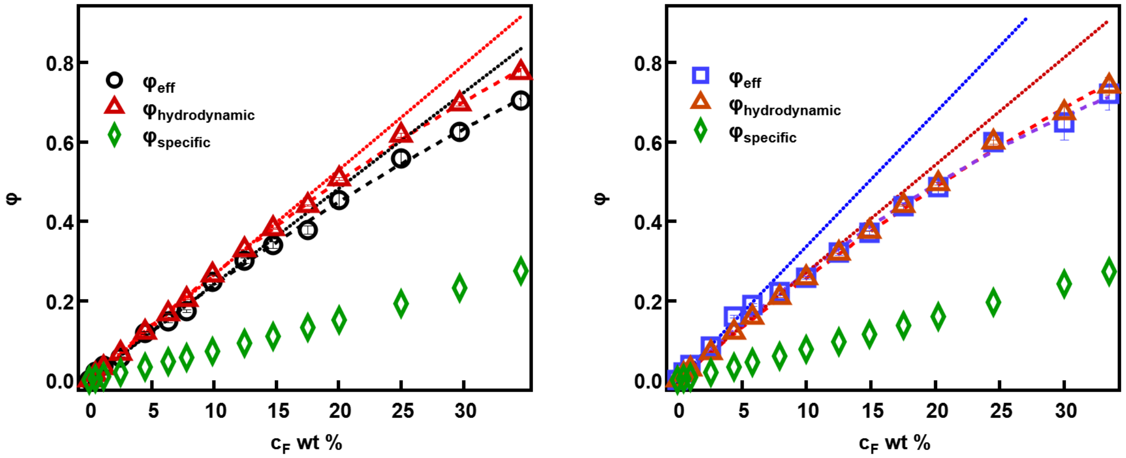

(a) (b)

Figure (3.4) **Effective volume fraction:** (a) Two alternative calculations of Ficoll volume fraction that account for bound water, ϕ_{eff} and $\phi_{\mathrm{hydrodynamic}}$ show a stronger increase with c_{F} than the traditional ϕ_s. Both (a) Ficoll-70 and (b) Ficoll-400 ϕ_{eff} and $\phi_{hydrodynamic}$ show a nonlinear increase for $c_{\mathrm{F}} > 10\%$.

The Ficoll volume fraction $\phi_{\mathrm{hydrodynamic}}$ is then obtained as

$$\phi_{\mathrm{hydrodynamic}} = \frac{V_{\mathrm{hydrodynamic}}}{V_{\mathrm{hydrodynamic}} + (1 - f_b^{\mathrm{HDO}})V_{D_2O}}. \tag{3.10}$$

These two distinct approaches of estimating the volume fractions, shown in Figure 3.4 (a) and (b), are remarkably consistent with each other, and yield much larger volume fractions than the bare polymer volume fraction ϕ_s. The ratio of $\frac{\phi_{\mathrm{hydrodynamic}}}{\phi_{\mathrm{eff}}}$ is 1.13 ± 0.01 for Ficoll-70 and 1.011 ± 0.004 for Ficoll-400. This gives us confidence that the true volume occupancy of the Ficoll must exclude the Ficoll-bound water from the accessible solvent free volume, and under crowding conditions, the volume occupancy is *not* 30 % *but* 65-70 %, as seen from the high-concentration values of both $\phi_{\mathrm{hydrodynamic}}$ and ϕ_{eff}. Moreover, while ϕ_s shows a linear dependence on the concentration, c_F, both the ϕ_{eff} and $\phi_{\mathrm{hydrodynamic}}$ is seen to increase nonlinearly beyond

$c_{\mathrm{F}} \sim 10 - 15\%$, roughly consistent with overlap concentrations determined using suspension viscosity measurements both in this work (Figure 3.3(b)) and elsewhere [89], of 150 - 250 $\frac{g}{L}$ ($\approx$ 13 - 16 % $\frac{w}{w}$). Table A.1 in the Appendix shows the weight fractions c_{F} of Ficoll-70 and Ficoll-400 investigated here and corresponding volume fractions ϕ_s, $\phi_{\mathrm{hydrodynamic}}$, ϕ_{eff}.

Relaxation: Next, we examine if the constrained environment for the solvent molecules, implied by the above diffusion measurements, is borne out by NMR transverse relaxation measurements, which are known to be strongly affected by the environment. Relaxation measurements report on nanosecond-to-picosecond molecular rotational correlation times, while diffusion reports on millisecond-scale translational diffusion: these measurements are thus very independent and yet performed on the same samples. Shown in Figure 3.5 are the transverse relaxation rates R_2 for Ficoll-70 and Ficoll-400 as a function of ϕ_{eff}. These rates have a value of about 2 (1/s) at $\phi_{\mathrm{eff}} = 0$, but have increased by an order of magnitude when $\phi_{\mathrm{eff}} = 0.4$ ($\approx$ 15 %) for Ficoll-70 and by $\phi_{\mathrm{eff}} = 0.25$ ($\approx$ 10 %) for Ficoll-400, and by another order of magnitude at $\phi_{\mathrm{eff}} = 0.7$. These numbers are roughly consistent with overlap concentrations of 13 to 16 % $\frac{w}{w}$) determined using suspension viscosity measurements. We also examine directly the ^{2}H spectra in the deuterium channel (shown in Supplementary Information Figure A3), for $c_{\mathrm{F}} = 1\%$, 15% and 35%. The significant broadening seen for the latter samples is consistent with a confined environment.

Ficolls are super-hydrated: The NMR results consistently indicate that the Ficolls are super-hydrated. The water and Ficoll diffusion coefficients enable us to obtain a realistic Ficoll volume fraction, and the HDO relaxation confirms that the average environment experienced by the water is severely constrained in the crowding limit. It is instructive to obtain the ratio of the water bound to each particle to

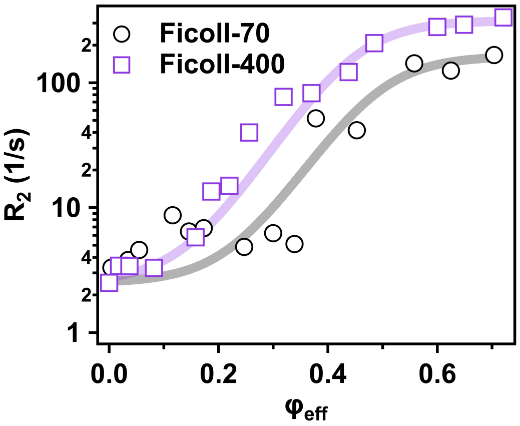

Figure (3.5) **NMR transverse relaxation:** ^1H transverse relaxation rates of solvent molecules, R_2 shows a dramatic increase, above $\phi_{\text{eff}} = 0.4$ for Ficoll-70 and above $\phi_{\text{eff}} = 0.25$ for Ficoll-400. Representative ^{2}H D_2O spectra, shown in Figure A3 of the Appendix, also show a significant broadening with increasing concentration, indicating a increasingly confined environment.

the incremental volume added to the solution by adding a particle. This ratio can be obtained from the individual terms in Equation 3.7. For Ficoll-400, this ratio decreases with increasing concentration from 3 to 2.4; for Ficoll-70 this ratio is 2.4. Thus, at any concentration, the water bound to Ficoll contributes 2.5 to 3 times the particle volume as does the polymer. This is analogous to similar realizations of a polymer-particle duality in the polymer microgel literature [86]. In PNIPAM microgels [98, 99] the particles hold a significant amount of water; up to 60 % of the particle volume is water, and microgels with lower crosslink density provide stronger confinement (collapse more) under strong osmotic stress. In the case of the Ficolls, Ficoll-400 is likely to have a more extended fuzzy shell than Ficoll-70, and thus, analagous to the the above phenomenon in microgels, Ficoll-400 show stronger signs of water confinement (larger R_2).

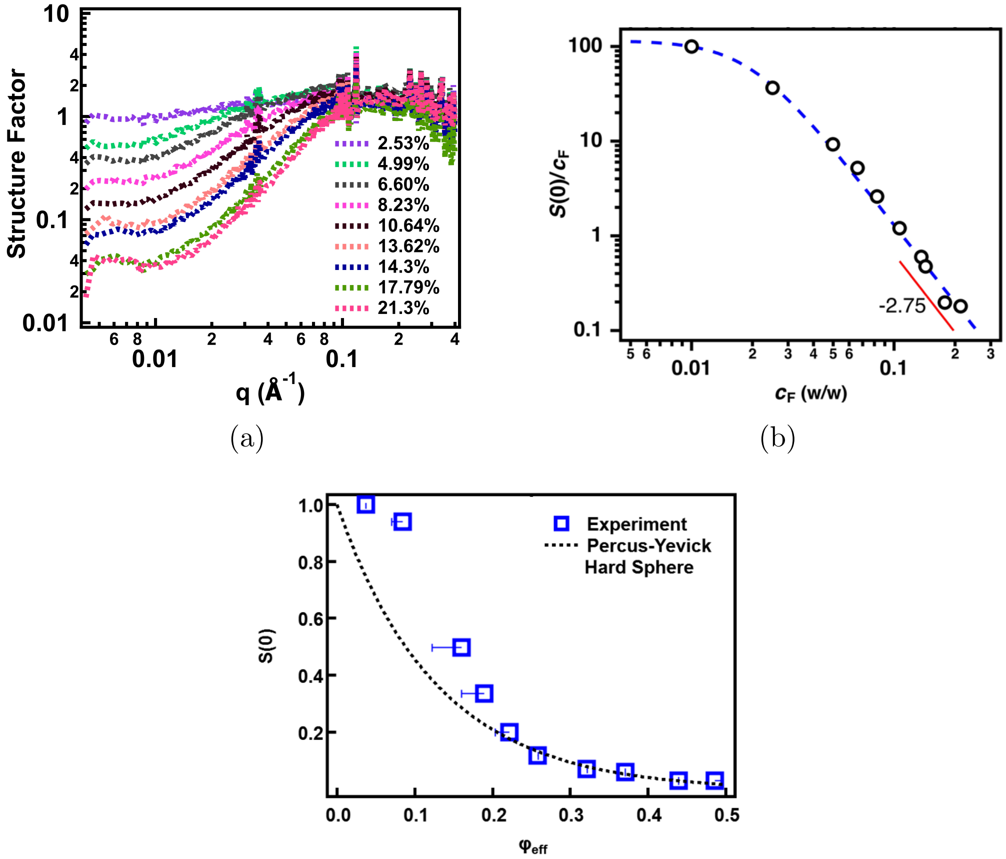

(a) (b)

(c)

Figure (3.6) **SANS structure factors:** (a) Structure factor of Ficoll-400 obtained as the ratio of neutron scattering intensity to the form factor, assuming a concentration-independent form factor. (b) Concentration-scaled structure factor of Ficoll-400 in the $q \to 0$ limit, $S(0)/c_{\mathrm{F}}$, which is a dimensionless osmotic compressibility. Error bars are close to the symbol size. (c) $S(0)$ plotted against ϕ_{eff} and compared with the hard-sphere (Percus-Yevick) values.

3.4 SANS structure factors: Ficolls are soft

We now obtain the structure factor of Ficoll-400 suspensions, shown in Figure 3.6, by dividing the neutron scattering intensity from the Ficoll suspensions by the form factor. It has to be noted that the ${f_b}^{\mathrm{HDO}}$ increase is only linear with Ficoll concentration, and the specific relaxation rates are only independent of Ficoll-400 concentration up to 10 % $\frac{w}{w}$ ($\phi_{\mathrm{eff}} \sim 0.2$). We interpret this regime as the dilute regime where the particle-particle interactions can be neglected. Therefore, in this regime $S(q) = \frac{I(c_{\mathrm{F}})}{I_{\mathrm{dil}}}$ is the true structure factor, where $I(c_{\mathrm{F}})$ is the neutron scattering intensity from the Ficoll sample and I_{dil} is Ficoll form factor. Beyond 10 % $\frac{w}{w}$, the form factor could be a function of the concentration and, in our experiments, the structure factor is not separable from the form factor; nevertheless, we can still extract the zero-q extrapolation of the structure factor (since the form factor is 1 at zero q).

Figure 3.6(b) shows $S(0)/c_{\mathrm{F}}$ as a function of c_{F}, where $S(0)$ is the extrapolation of $S(q)$ to zero q. This quantity can be identified as a (dimensionless) osmotic compressibility χ, since $\chi = \frac{S(0)}{k_B T c_{\mathrm{F}}}$. Following Cohen *et al*, we might expect the osmotic pressure to follow a crossover scaling form that is a sum of the dilute concentration dependence ($\Pi \sim c_{\mathrm{F}}$) and semi-dilute concentration dependence ($\Pi \sim c_{\mathrm{F}}^{9/4}$). Since $\chi \sim 1/(d\Pi/dc_{\mathrm{F}})$, we can therefore fit the osmotic compressibility to a form

$$\frac{S(0)}{c_{\mathrm{F}}} \sim \frac{D}{1 + (c_{\mathrm{F}})^z}. \tag{3.11}$$

At low concentration, this form should have concentration-independent asymptote, and this indeed appears to be the case, as seen by the fit to the crossover form at low c_{F}. At higher concentrations, for a polymer in semi-dilute solution, one expects $z = 9/4 - 1 = 1.25$ [13]. We, however, obtain $z = 2.74 \pm 0.01$.

Given this lack of agreement in the more concentrated regime, one might wonder if, while the Ficoll single particle form factor is closer to a polymer than a colloid, perhaps the Ficolls in their quiescent state interact with other Ficolls more like a particle than like a polymer? To this end, we replot the $S(0)$ against the effective volume fraction ϕ_{eff}. The corresponding value of $\phi_{\text{hydrodynamic}}$ is shown as a one-sided uncertainty in ϕ_{eff} - the values are provided for easy comparison in Appendix Table 1. It is seen in Figure 3.6(c) that this dependence, deviates significantly from the Percus-Yevick (PY) hard-sphere form at low ϕ_{eff} but approaches it asymptotically at higher ϕ_{eff}.

One potential reason for the osmotic compressibility being larger than the hard-sphere value is weak, short-ranged attractive interactions: this can be examined *via* computer simulation. Such attractions would be less relevant once the Ficolls are in contact: this would roughly be consistent with the approach to hard-sphere-like behaviour at high ϕ_{eff}.

3.5 Conclusion

Using multiple complementary experimental techniques, rheology, SANS and NMR diffusometry and relaxometry, we have investigated the structure of a model polysaccharide macromolecular crowder of two sizes, Ficoll-70 and Ficoll-400. For both Ficoll-70 and Ficoll-400, the viscosity of the suspensions follow a crossover form from linear dependence of the concentration c_{F} in dilute solution, to de Gennes scaling for a reptating polymer in concentration solution [88]. The prefactor to this crossover scaling form, known as the Huggins constant, is identical to the previously reported value for solutions of (non-crosslinked) polysaccharide polymer with a single backbone.

The SANS form factor of Ficoll-400 does not exhibit a sphere-like character but is rather well-fit to the Debye model for a linear Gaussian polymer, and the ratio $R_g/R_H \sim 1.52$ which is within the range of values 1.44 - 1.59 expected for a Gaussian polymer and/or polymers in good solvent [93]. This non-compact polymeric structure could account for non-monotonic enzyme folding kinetics with Ficoll as the crowding agent [100, 101, 102]. There is some complexity in this: the volume accessible for macromolecules of size comparable to R_g is much smaller than the volume accessible to smaller molecules (like the substrate molecule in enzyme kinetics studies).

The concentration-dependent reduction in the observed self-diffusion coefficient of the trace HDO molecules in D_2O helps us estimate the effective Ficoll volume fraction, which includes particle-associated water. This water is "bound" only in a statistical sense, because on the time scales of the NMR diffusion experiment (tens of milliseconds), an individual water molecule exchanges rapidly between the free and the particle-associated state. The bound water fraction is large, approaching $f_b = 0.6$ in the crowding limit. Independently, and consistently, we see a sigmoidal rise in a dimensionless specific transverse relaxation rate from zero (the value for free water, by definition) towards a plateau value that is consistent with a highly constrained environment. We identify a non-linear growth of the Ficoll-400 bound water fraction (f_b) with increase in c_{F}, while f_b for Ficoll-70 increases linearly. This suggests that while the water content per particle is roughly constant as a function of c_{F} for Ficoll-70, it decreases a bit in Ficoll-400 (due either to particle overlap or particle compression).

The increase in Ficoll-bound water, obtained *via* long-time diffusion measurements, are completely consistent with increasing NMR relaxation rates, which reflect short-time rotational motions. In the future, one could also use Raman scattering experiments to evaluate the nature of Ficoll-bound water under crowding [103] and to understand the difference in the magnitude of specific relaxation rates for Ficoll-70 and Ficoll-400 above the identified overlap concentrations.

Volume fractions traditionally calculated using the Ficoll partial specific volume, in contrast, simply yield the additional solution volume due to the Ficoll polymer; they do not capture the hydrated volume occupied by the Ficolls. We report, for the first time, an effective volume fraction for Ficoll that reflects a particle volume which includes Ficoll-bound water and more importantly, a solvent volume that excludes the Ficoll-bound water. In the crowding limit the effective volume fraction is not between 20 and 30%, but between 60 and 70%; this estimate is totally consistent with the polymer-like rheology observed, which implies that Ficolls interpenetrate and/or deform during shear.

From this multi-technique study, we say, conclusively, that Ficolls are not prototypical colloid-like excluded-volume crowders, that they occupy a hydrodynamic volume that consists of 2.5-3 times as much water as polymer, and that their structure is consistent with that of a Gaussian polymer: at the very least, it is a highly non-compact object. There is an interesting parallel between these findings and findings of polymer-colloid duality in the microgel literature [86]. Similar challenges are also faced in understanding structure and dynamics in globular protein solutions [50, 87].

Finally, we discuss two examples of the impact of the current work. In their study of polymer diffusion in Ficoll-70 solutions, Palit *et al.* identify a characteristic concentration, $c^\star$ for poly(ethylene glycol) (PEG) molecules, a concentration below which the diffusion coefficient of PEG is independent of the PEG concentration. This characteristic concentration, $c^\star$, however, decreases as a function of the Ficoll concentration and reaches a plateau beyond a Ficoll-70 volume fraction of 0.1 (Figure 2 (c) of reference [28]). However, the volume fractions were estimated using the specific volume of the Ficoll-70 suspensions, and is equivalent to the ϕ_s in Figure 3.4(a) in this chapter; this thus corresponds to $\phi_{\text{eff}} = 0.25$. Similarly, Dhar *et al* [100] studied protein folding time scales in Ficoll-70 solutions as a function of the concentration of Ficoll-70. They observed sharply non-monotonic behaviour: first a decrease in the relaxation time as a function of Ficoll-70 concentration, and then, above 100 mg/ml, a sharp increase. The bottom of this "inverse chevron" was calculated to occur at a volume fraction of 0.1 (Figure 2 B of ref [100]). Again, this corresponds to a ϕ_s of 0.1, but a ϕ_{eff} of 0.25. This picture is rather consistent with our measurements of the osmotic compressibility of Ficoll-70, where we observe that beyond $\phi_{\text{eff}} \approx 0.2$, the osmotic compressibility is closer to that of hard spheres. Thus we strongly believe that, our results will affect many past studies in which the volume fraction of Ficoll is considered to be the independent parameter. Particle-based simulations of crowding that require volume fraction as an input will need to consider Figure 3.4.

Chapter 4

Self-diffusion and relaxation of bovine serum albumin and phytoglycogen nanoparticle solutions

In the previous chapter, we have identified that the self diffusion of water molecules is a sensitive technique to examine the true hydrodynamic volume occupied by macromolecules in a suspension. In this chapter, we evaluate the self diffusion and NMR relaxation dynamics of water molecules in bovine serum albumin solution and phytoglycogen suspensions as well as the self diffusion coefficients of these macromolecules.

Bovine serum albumin (BSA) is a single domain globular protein crowder molecule extensively used as a biological crowder molecule in macromolecular crowding studies [104, 105]. Ota *et al.* have reported a Raman spectroscopy study on the behavior of bovine serum albumin in crowded environments [103]. From the Raman scattering experiments of BSA solution, the authors identify three different water species at the physiological pH; bulk water, protein-hydrated water, and the interfacial water. They observed reduction in the bulk water and an increase in the protein hydrated water with an increase in BSA concentration. Interestingly, they report that the reduced concentration of interfacial water reduces to zero at 80 mg/mL of the protein concentration but in this range, the sum of protein-hydrated and interfacial water concentrations is constant. This suggests strongly that one consider a simple picture with two species: bulk water and bound water. The fraction of bulk water is roughly constant in dilute solution and up to 80 mg/mL at a value of 0.89 ± 0.01, but decreases steadily to ≈ 0.75 by 300 mg/mL. The authors do not observe changes in the secondary structure of the protein molecule even at higher concentration regime.

Roosen-Runge *et al.* have performed small angle X-Ray scattering on BSA solutions, and report that the form factor resembles the structure of an ellipsoidal colloid [48]. This observation is consistent with the form factor obtained through small angle neutron scattering experiments by Bendedouch *et al.* [106]. By performing quasielastic neutron back scattering, Roosen-Runge *et al.* report the self diffusion coefficient of BSA in crowding conditions and observe that at the biological volume fractions, the self diffusion coefficient decreases with increase in volume fraction. Moreover they argue that the general features of the solution can be captured effectively assuming the colloidal hard particle model of the suspensions [48].

In general, the excluded volume effect introduced by the colloidal crowders always stabilizes the probe protein structure [107, 108]. BSA, however, is reported to exert varying effects on the stability of the probe protein depending on the pH and concentration, thus raising question on the applicability of colloidal picture of BSA crowders. Sarangapani *et al.* have reported that the definition of volume fraction in

BSA is inappropriate, and invoking the hydrodynamic volume of the molecule leads to the incorrect prediction of BSA as a rigid colloidal particle [50]. They report that calculating volume fraction based on pH dependent specific volume rightly captures the features of the suspension properties at a wide range of pH. They show that phenomenological models based on excluded volume such as the Krieger-Dougherty model for hard-sphere suspensions, or the Russel model which accounts for particle surface charges, are insufficient to explain the viscosity of BSA at the the probed concentrations, and pH [49].

BSA is widely used as a model excluded volume crowder in macromolecular crowding studies. In this chapter, we report the self diffusion coefficient of the BSA crowder molecules and water molecules in the BSA suspensions of different concentrations at physiological pH investigated by diffusion NMR experiments. We extract the fraction of BSA bound water molecules and employ that to construct a volume fraction for BSA molecules.

Next, in this chapter, we examine the diffusion coefficient of phytoglycogen dendrimers (and of the solvent) in the same way as BSA. Based on prior viscosity measurements [109], these phytoglycogen particles are a promising future candidate for *in vitro* macromolecular crowding studies. Phytoglycogens are natural nanoparticles that act as glucose storing units in some plants. The structure of phytoglycogen nanoparticles is similar to that of dendrimers where one unit consists of regularly branched glucose chains. Nickels *et al.* test several models for the form factor of phytoglycogen particle and conclude that a best fit is obtained by modelling the particle as a uniform sphere [51]. Further, they have successfully applied hard sphere structure factor model up to 25 % $\frac{w}{w}$ and estimated the interparticle distances. Their study identifies two species of water molecules, the phytoglycogen bound water and the bulk water. They conclude that phytoglycogen is an efficient water retention agent. Shamana *et al.* on the other hand show that phtoglycogen particles are rather soft and they report the osmotic compressibility of the suspension [109]. The compressional value for phytoglycogen they report, 15 kPa, is close to the value of microgels and star polymers. They also calculate an effective volume fraction for phytoglycogen nanoparticles, which exceed significantly beyond the hard sphere glass transition volume fraction, indicating the softness of the particles. Further, by performing rheological measurements for a wide range of concentrations, they identify that until 20 % wt, the phytoglycogen suspensions show Newtonian behavior and beyond that a shear thinning liquid like behaviour. They model the rheology of the suspensions using the Vogel–Fulcher–Tammann (VFT) model of glassy dynamics.

In this chapter, we investigate and compare the results of self-diffusion of BSA and of phytoglycogen nanoparticles obtained in the millisecond time window, the self-diffusion of water in the same suspensions, and thereby the fraction of water molecules associated with the phytoglycogen nanoparticles and for BSA. We also obtain relaxation rates for the water (probing rotational correlations at much shorter timescales) for all these suspensions.

4.1 Materials and methods

We disperse the phytoglycogen particles in D_2O by homogenizing the sample at 11000 rpm using a 7mm homogenizer probe for 3 minutes using a Fisher brand homogenizer. The phytoglycogen nanoparticles were a gift from Mirexus Biotechnologies. This homogenization is repeated 5 times with an interval of 1 minute between each stirring. The sample is then loaded to a 4mm tube which is inserted to a 5 mm NMR tube for

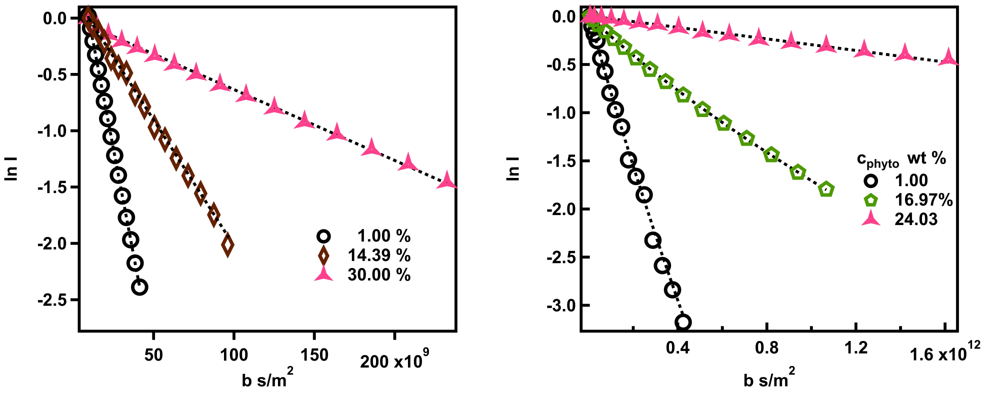

(a) (b)

Figure (4.1) **PFG-NMR:** Natural logarithm of NMR signal intensity decay against gradient parameter b (defined in equation 2.24) shown for three concentrations for (a) BSA (b) Phytoglycogen.

NMR experiments. We disperse the BSA in 0.1 M phosphate buffer solution. All the experiments were performed at 25^{o}C.

4.2 Results and Discussion

The NMR signal intensity decays mono-exponentially for BSA while a non mono-exponential decay is observed for phytoglycogen particles as shown in Figure 4.1 (a) & (b). In our experiments, the time between the first two pulses in PFG-STE is set to $\delta = 2\ ms$ and the diffusion time is $\Delta = 50\ ms$ (parameters in equation 2.24). We fit the NMR intensity decay of phytoglycogen to a bi-exponential function as in equation A.1 and obtain the average self diffusion using equation A.2. The NMR intensity decays mono-exponentially for HDO in both BSA and phytoglycogen suspensions.

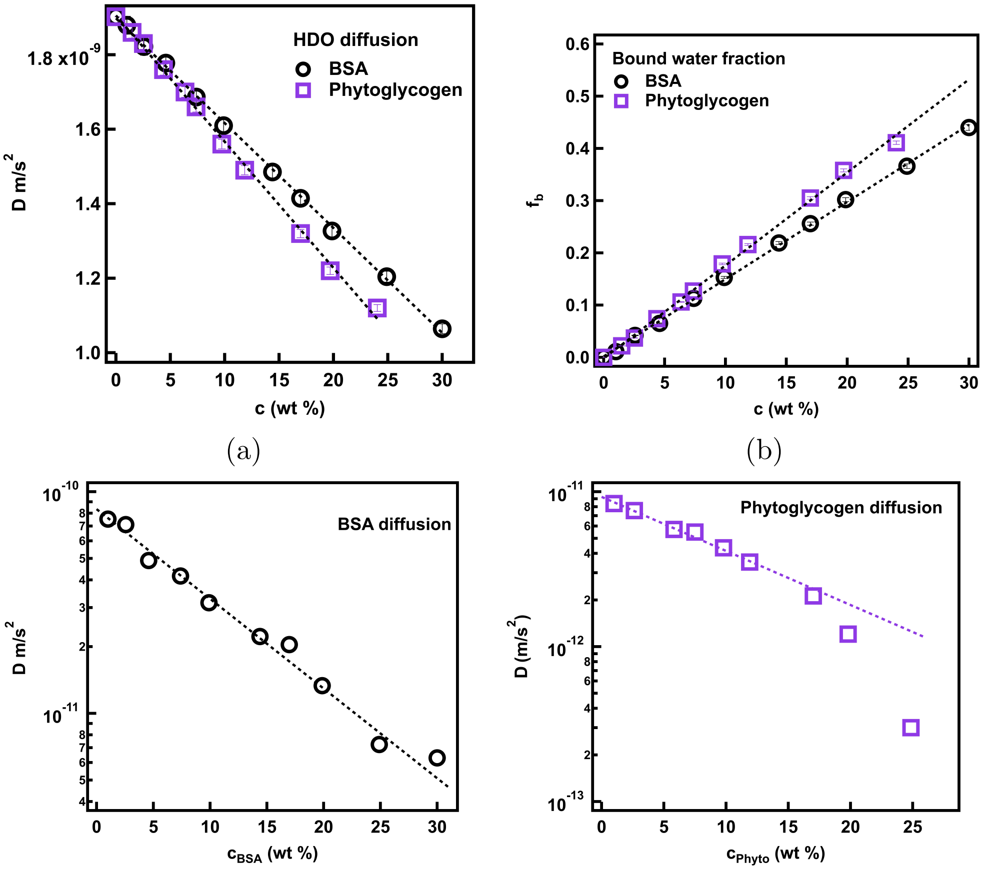

(a) (b)

(c) (d)

Figure (4.2) **PFG-NMR:** (a) Self diffusion coefficient of HDO molecules decrease linearly in BSA and Phytoglycogen suspensions. (b) Fraction of bound water show a linear increase with suspension concentrations for BSA and phytoglycogen. (c) An exponential decrease in self diffusion coefficient with concentration, c_{BSA}, is observed for BSA. (d) The self diffusion coefficient of phytoglycogen deviates from exponential decrease around 15 % where the suspension property is reported to change from Newtonian to shear thinning.

Table (4.1) BSA volume fractions using different methods: the mass fraction c_{BSA} (as per equation 3.1), and the volume fractions based on polymer specific volume (equation 3.7), polymer specific volume accounting for bound water (equation 3.8) and particle hydrodynamic volume accounting correcting for bound water in the solvent volume (equation 3.10).

c_{BSA} ($\% \frac{w}{w}$)	ϕ_s	$\phi_{\mathrm{hydrodynamic}}$	ϕ_{eff}
0	0	0	0
1	0.007	0.027	0.017
2.57	0.018	0.05	0.058
4.59	0.034	0.082	0.095
7.39	0.054	0.116	0.16
9.9	0.073	0.173	0.214
14.39	0.109	0.216	0.303
16.97	0.13	0.26	0.351
19.87	0.153	0.334	0.408
24.9	0.195	0.417	0.489
30	0.239	0.447	0.573

The self diffusion coefficient of HDO molecules decreases linearly with concentration for both BSA and phytoglycogen nanoparticles in D_2O as shown in Figure 4.2 (a). Using equation 3.5, we extract the fraction of particle bound water and we observe a linear increase of f_b with suspension concentration for both BSA and phytoglycogen as shown in Figure 4.2 (b). The self diffusion coefficient of BSA and phytoglycogen particles are shown in Figure 4.2 (c) and (d). The self diffusion coefficient decreases exponentially with a characteristic concentration of 10.99 ± 0.76 % for BSA and 11.74 ± 0.87 % for phytoglycogen. Interestingly, for all the crowder suspensions studied in this thesis – Ficoll-70 (black circles in Figure 3.3(b)), Ficoll-400 (purple squares in Figure 3.3(b)), BSA (Figure 4.2(c)), and phytoglycogen (Figure 4.2(d)) – the decrease in D with concentration is exponential:

$$D = D_0 \exp(-c/c_2). \tag{4.1}$$

In addition, the characteristic concentrations c_2 are all around 10-12 %. However, a marked deviation from the exponential decrease in self diffusion coefficient is observed for phytoglycogen above 20 %. Interestingly, this is the concentration where the rheological properties of the suspension is report to change from Newtonian to non-Newtonian shear thinning behaviour [109], and indeed the decrease in D beyond this concentration is even sharper. A smaller, but noticeable, deviation from the exponential decrease of self diffusion coefficient was also observed for Ficoll-400 above the overlap concentration (Figure 3.3 b).

By extrapolating the exponential fit to the self diffusion coefficient, we obtain $D_0 = (8.34 \pm 0.27) \times 10^{-11}$ m^2/s for BSA and $(9.26 \pm 0.21)\times$ 10^{-12} m^2/s for phytoglycogen. The estimated hydrodynamic radius using the Stokes-Einstein equation is R_H = 2.93 ± 0.09 nm for BSA and 24.46 ± 0.60 nm for phytoglycogen. The specific volume of BSA is 0.735 ml/g [48]. The specific volume of phytoglycogen is not yet reported. We compute the effective and hydrodynamic volume fractions using equation 3.8 and 3.10 for BSA. The ϕ_{eff} deviates very slightly from linearity beyond 10-15 % while $\phi_{\mathrm{hydrodynamic}}$ and ϕ_s increases linearly as shown in Figure 4.3 (a). Table 4.1 shows the weight fraction and corresponding ϕ_{s}, $\phi_{\mathrm{hydrodynamic}}$ and ϕ_{eff} for BSA.

Next we compare the $\phi_{\mathrm{hydrodynamic}}$ and ϕ_{visc} for phytoglycogen nanoparticles. Shamana *et al*. estimated a volume fraction, referred to as ϕ_{eff} in reference [109] but as ϕ_{visc} here, as a product of concentration conversion factor, k and concentration c in w/w %: $\phi_{\mathrm{visc}} = kc$. They obtain the proportionality constant k by fitting viscosity measurements in the dilute limit to the Einstein-Batchelor equation (see, for example, Ref [110]), a procedure that is strictly only valid for hard spheres: from this, they report $k = 0.0353$. This volume fraction increases linearly with concentration as shown in Figure 4.3 (b). The $\phi_{\mathrm{hydrodynamic}}$, estimated from NMR experiments, on the other

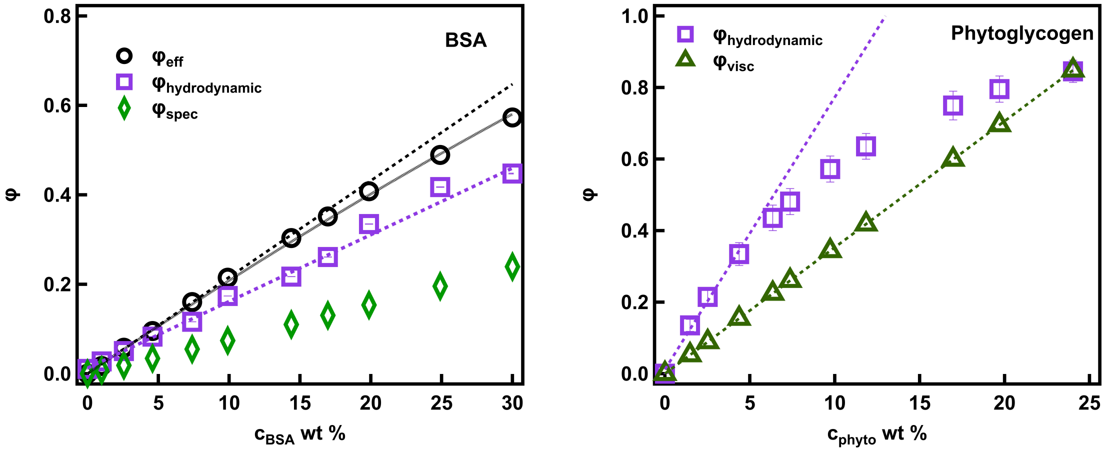

(a) (b)

Figure (4.3) **PFG-NMR:** (a) ϕ_{eff} for BSA increases non-linearly beyond 15 % while the $\phi_{\text{hydrodynamic}}$ almost increases linearly. (b) The $\phi_{\text{hydrodynamic}}$ for phytoglycogen show marked deviation from linearity beyond 5% while ϕ_{visc} defined by Shamana *et al.* [109] increases linearly.

hand, increases linearly only up to 5 % w/w. An experimental measurement of specific volume for phytoglycogen is not yet reported. Therefore, the calculation of ϕ_{eff} and ϕ_{s} for phytoglycogen is reserved for a future work. Table 4.2 shows the weight fractions and corresponding $\phi_{\text{hydrodynamic}}$ and ϕ_{visc} for phytoglycogen.

Relaxation: Transverse relaxation rates R_2 of the solvent molecules are good, independent indicators of the change in environment of the colloidal suspensions. Increase in relaxation rates indicates the increased constraint on molecular mobility. The R_2 for BSA increases linearly up to 30 % w/w. While we do not have a model for the transverse relaxation rates, the R_2 for phytoglycogen increases linearly up to 12 % and increases sharply thereafter. The corresponding hydrodynamic volume fraction, $\phi_{\text{hydrodynamic}}$, is ≈ 0.636, close to hard sphere packing fraction. Beyond this concentration, as mentioned earlier, it has been reported that the suspension is rheological properties change from Newtonian to shear thinning behaviour around this concentration [109]. It is notable that the water in its most confined state in

Table (4.2) Phytoglycogen volume fractions using different methods: the mass fraction c_{phyto} (as per equation 3.1), the particle hydrodynamic volume accounting correcting for bound water in the solvent volume (Equation 3.10) and ϕ_{visc}.

c_{phyto} (% $\frac{w}{w}$)	$\phi_{\text{hydrodynamic}}$	ϕ_{visc}
0	0	0
1.5	0.135	0.052
2.52	0.215	0.089
4.37	0.334	0.154
6.35	0.436	0.224
7.37	0.481	0.26
9.73	0.572	0.343
11.84	0.636	0.418
16.97	0.75	0.56
19.7	0.796	0.695
24.03	0.845	0.848

phytoglycogen has a relaxation rate $R_2 \sim 250$ (1/s), which is similar to the value in Ficoll-400 at the highest concentration.

4.3 Conclusion

In this chapter, we have evaluated the volume occupancy of BSA, a globular protein, and the phytoglycogen dendrimer. Two methods of taking water volumes into account in the volume fraction were presented in this thesis: both volume fractions, ϕ_{eff} and $\phi_{\text{hydrodynamic}}$ increase to a value above $\phi = 0.4$: ϕ_{eff} increases to 0.57 at $c_{\text{BSA}} = 30\%$, while $\phi_{\text{hydrodynamic}}$ increases to 0.45. The R_2 relaxation rates of HDO molecules in BSA solution increases linearly with concentration indicating increased constraints on the solvent molecules. The maximum value of R_2 is near 100 1/s, comparable to the value in Ficoll-70, but significantly lower than the value in Ficoll-400.

The self diffusion coefficient of BSA and phytoglycogen decreases exponentially

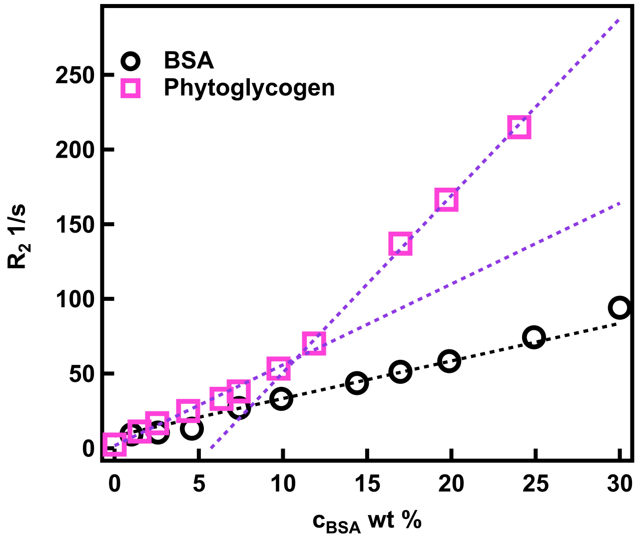

(a)

Figure (4.4) **PFG-NMR:** R_2 relaxation rate for HDO in BSA and phytoglycogen suspension increases with suspension concentration indicating the increased constraint on the HDO molecule.

with increasing concentration and we estimate a characteristic concentration of 10-12 %. A similar observation is also made for Ficoll nanoparticles. This is discussed in more detail in Chapter 5.

For phytoglycogen, we did not have sufficient quantities to obtain a partial specific volume $\bar{v}$, so we only obtained $\phi_{\text{hydrodynamic}}$. The hydrodynamic volume fraction for phytoglycogen show a linear dependence on c_{phyto} up to 5 % and a marked deviation from linearity at higher concentrations, being strongly sublinear: it nevertheless reaches a value of 0.85 at 25 % w/w. Shamana *et al.* have also reported an effective volume fraction which in this thesis is termed as ϕ_{visc}, because it is obtained by using the linear relation $\phi_{\text{visc}} = kc$ and obtaining the proportionality constant k by fitting viscosity measurements in the dilute limit to the Einstein-Batchelor equation, a procedure that is strictly only valid for hard spheres. ϕ_{visc} reaches 0.85 at 25 % w/w. However, the volume fraction, ϕ_{visc}, increases linearly until crowding conditions. Our work provides a self-consistent means to obtain a reliable volume fraction far from the dilute limit, and implies that phytoglycogen are also far softer than previously thought. The self diffusion coefficient of phytoglycogen show significant deviation from the exponential decay trend at around 15 % w/w.

The transverse relaxation rate, R_2, of HDO molecules in phytoglycogen suspensions increases linearly up to this concentration (identified as maximum hard-sphere random-close-packing fraction from $\phi_{\text{hydrodynamic}}$) and then a sharp increase indicating increased constraint on the solvent molecule mobility. Shamana *et al.* have reported that the phytoglycogen suspensions undergo a Newtonian to shear thinning behaviour at this concentration. We find that the R_2 relaxation measurements of solvent molecules is an independent method to obtain qualitative information on the suspension properties. A sharp increase in the R_2 for HDO molecules was also observed for Ficoll-400 at a concentration where the diffusion of Ficoll-400 shows a noticeable deviation from the exponential dependence on the concentrations (Figure 3.3 (b)).

Chapter 5

Conclusions and future work

5.1 Conclusions

Biological cells are the fundamental units of all living species [111]. Inside living cells, there exist a mixture of macromolecular entities at a high concentration performing different actions to sustain normal function. These molecules are under the simultaneous action of multiple interaction potentials which makes the study interesting but challenging. Excluded volume interactions are a fundamental interaction in which a molecule makes its occupancy space unavailable for other molecules to occupy. This entropic interaction is always present regardless of any other physical or chemical properties of the molecule [112]. A broad range of research has been previously reported on the effects of excluded volume interactions induced by crowder molecules on the conformations of molecular probes [113, 114, 115, 116, 117, 118, 119]. However, while the mass fractions are easy to measure, estimating excluded volume in experiments has been challenging.

In this thesis, we employ multiple experimental techniques to obtain reliable information about crowder excluded volume. We report a simple but efficient method to determine the volume occupancy of the crowder molecules in aqueous suspensions, which in principle can be applied to any system for measuring the total free volume available for molecules to occupy. In our formulation, we estimate the self diffusion coefficient of the solvent and crowder using pulsed field gradient nuclear magnetic resonance spectroscopy. From the solvent and solute diffusion coefficients, and assuming that the solvent (water) either diffuses freely or is bound to the crowder, we can obtain a robust estimate of the fraction of bound water. An independent probe of the water environment, relaxometry, yields results very consistent with diffusometry.

We then estimate the volume of the suspensions using two different methods. In one method, we compute an effective volume, V_{eff} based on both the product of the solute specific volume and mass, and the volume of solute bound solvent molecule. In another method, we obtain the hydrodynamic volume obtained in the dilute limit, but, we remove the overestimation of solute bound solvent volume using the concentration dependence of solute bound water. This is referred to as $V_{\text{hydrodynamic}}$. The volume fraction of the suspensions, then, is the ratio of calculated solute volume and the solution volume. As an independent check, we also measure their NMR transverse relaxation rates (which are related to short time motions) as a function of the concentration, and find results that are consistent with the diffusion measurements (which probe very long time motions) and the bulk rheological properties of the suspension.

For Ficoll-400 and Ficoll-70 crowder molecules, the volume fractions estimated following the two approaches, ϕ_{eff} and $\phi_{\text{hydrodynamic}}$, yield self-similar results. Interestingly, our observation reveals that the volume occupancy of these suspensions is not 30 to 40 % at crowding conditions rather they reach 65-70 %. Moreover, the volume fractions increase in a non-linear fashion beyond a concentration which is identified as the overlap concentration of the suspension from rheological measurements. These observations conclusively say that Ficoll is highly porous rather than a hard sphere, and the volume it excludes is largely determined by the water it holds: the pervaded volume of Ficoll has 2.5 times more water than polymer.

Is Ficoll colloid or polymer? Our SANS experiments reveal that the form factor resembles a Gaussian polymer chain. The self diffusion coefficient of Ficoll (obtained by NMR) follows an exponential decrease, but shows a small but noticeable deviation beyond the overlap concentration for Ficoll-400. The relative viscosity of the suspension increases linearly in the dilute regime and follows a power law beyond that, giving a de-Gennes coefficient of $\frac{15}{4}$ for a reptating polymer. All the above indicate polymer-like behaviour. Furthermore, the NMR relaxation of HDO molecules in the Ficoll suspension follow a sigmoidal growth indicating increased constraint on the molecular mobility. This, coupled with the quantitation of bound water, clearly hint that if Ficoll is a colloid, it is a highly porous one. The osmotic compressibility obtained as the structure factor $S(q \to o)$ as the wave vector tends to zero deviates from the Percus-Yevick model for hard-sphere colloids. However, it also does not follow the scaling behaviour expected for a linear polymer in good solution, in sharp contrast with the agreement of the viscosity to de Gennes scaling, and in contrast to the fitting of the form factor to a Gaussian polymer. Ongoing simulation work in the group of Dr. Wallin [120] shows that the experimental osmotic compressibility can successfully be modelled using a combination of softness and attractive interactions. The detailed investigation on the structure of Ficoll molecules using multi-technique experimental studies reveal that Ficoll is perhaps more *polymer like* than *colloid like*, but one must account for some degree of “colloid-like” compactness imparted to the Ficoll by its internal crosslinks.

Investigations on solutions of the protein crowder molecule BSA shows that while ϕ_{eff} increases linearly, $\phi_{\text{hydrodynamic}}$ shows a non-linearity beyond 10-15 %. The self diffusion coefficient of BSA molecules follow an exponential decrease in trend until crowding conditions. The NMR R_2 relaxation follows a linear increase with suspension concentration. For the phytoglycogen dendrimer, the $\phi_{\text{hydrodynamic}}$ is non-linear with concentration above 5 % w/w and the NMR R_2 relaxation increases linearly with suspension concentration until the maximum hard-sphere packing fraction obtained using hydrodynamic volume fraction and then shows a sharp increase. The self diffusion coefficient of phytoglycogen also shows a marked deviation from the exponential decay. This concentration is previously identified as the concentration at which the suspension properties changes from Newtonian to non-Newtonian shear thinning suspensions.

The work of Palit *et al.* [28] showed that the self-diffusion coefficient of the polymer polyethylene glycol in water exhibited an exponentially decreasing concentration dependence. The work of Rozenfeld [121] and Dzugutov [122] proposed an exponential relationship between atomic diffusion and the excess entropy. Thorneywork *et al.* [123] make a direct connection between long-time self-diffusion coefficients and particle concentration: they too found an exponential dependence in both Monte Carlo simulations and experiments, albeit in 2 dimensions and for hard-sphere colloids. As a result of the work in this thesis, we see that this exponential dependence is widely valid: not just for the linear polymer PEG, but for more compact Ficolls and for phytoglycogen nanoparticles (up to a high volume fraction), and as well for the globular protein BSA.

5.2 Future directions

While this thesis provides convincing evidence for two co-existing species of water, it would be exciting to have direct spectroscopic evidence. A systematic Raman scattering experiment on these suspensions would be an efficient way to quantify the different kinds of water and their relative populations. This study will help us in understanding the reason for the higher magnitude of relaxation rates of water at the highest crowder concentration, seen for Ficoll-400 and phytoglycogen as compared with Ficoll-70 and BSA. Indeed Ota *et al.* suggest three different water species in BSA suspensions [103]. Comparison of the spectroscopic signature in different crowders can help verifying this point. In addition, Brillouin scattering experiments can be used as a quiescent probe of the rheological properties of the suspensions [124].

A neutron spin echo experiment would provide a way to access information about short time motions. These experiment will provide a complete understanding of the Ficoll system which will be a valuable source for any future macromolecular crowding studies. We conclude with the observation that the study of macromolecular crowding can greatly benefit from the use of multiple experimental techniques, diffusion NMR, NMR relaxation, rheology, SANS and neutron spin echo along with Raman/Brillouin scattering studies.

Appendix A

A.1 Ficoll volume fractions using different methods

We disperse the required amount of Ficoll (g) in 1 mL of D_2O which weighed 1.1 g. The concentration of the Ficoll suspension is then defined as in equation 3.1. Table A.1 below shows the volume fraction of Ficoll estimated through three different methods. In one method, we calculate volume fraction based on the Ficoll-70 specific volume 0.65 ml/g and Ficoll-400 specific volume 0.67 ml/g [89, 84] using equation 3.7. In another method, we estimate the volume fraction using polymer specific volume accounting for bound water using Equation 3.8. Using equation 3.10, we report the volume fraction estimated using particle hydrodynamic volume accounting correcting for bound water in the solvent.

Table (A.1) Ficoll volume fractions using different methods: the mass fraction c_{F} (Equation 3.1), and the volume fractions based on polymer specific volume (Equation 3.7), polymer specific volume accounting for bound water (Equation 3.8) and particle hydrodynamic volume accounting correcting for bound water in the solvent volume (Equation 3.10).

Ficoll-70				Ficoll-400			
c_{F} (% $\frac{w}{w}$)	ϕ_s	$\phi_{\mathrm{hydrodynamic}}$	ϕ_{eff}	c_{F} (% $\frac{w}{w}$)	ϕ_s	$\phi_{\mathrm{hydrodynamic}}$	ϕ_{eff}
0	0	0	0	0	0		
0.45	0.003	0.014	0.020	0.49	0.004	0.013	0.018
1.13	0.008	0.030	0.035	1.00	0.007	0.027	0.038
2.53	0.018	0.067	0.056	2.57	0.028	0.069	0.083
4.46	0.032	0.119	0.116	4.4	0.033	0.120	0.158
6.34	0.046	0.166	0.146	5.83	0.044	0.158	0.187
7.78	0.057	0.203	0.173	7.93	0.060	0.208	0.22
9.89	0.073	0.263	0.247	9.99	0.076	0.257	0.256
12.45	0.093	0.328	0.3	12.53	0.096	0.320	0.319
14.75	0.110	0.382	0.339	14.88	0.115	0.375	0.37
17.53	0.132	0.440	0.078	17.65	0.137	0.439	0.439
20.01	0.152	0.507	0.453	20.36	0.159	0.495	0.486
25.01	0.193	0.617	0.558	24.66	0.195	0.600	0.6
29.7	0.232	0.696	0.625	30.18	0.243	0.673	0.649
34.6	0.274	0.774	0.704	33.69	0.274	0.74	0.722

A.2 Pulsed-field-gradient NMR experiments

A diffusion probe with a maximum field gradient 1800 G/cm is used to perform pulsed-field-gradient NMR (PFG-NMR) diffusion measurements using the stimulated echo pulse sequence [56]. (in the gradient range $g = 0 - g_{\max}$ G/cm, where $g_{\max}$ ranges from 100 G/cm at low c_{F} to 1400 G/cm for 35 %).

Figure A1 (a) shows the decrease of PFG-NMR signal intensity for Ficoll-400 for 3 different concentrations as a function of applied gradient parameter, b, given by Equation 2.24. For single-component systems, the signal attenuation is a simple exponential decay, and the diffusion coefficient is obtained as the slope of the linear fit to the natural logarithm of the intensity vs the gradient parameter b. Since we observe nonlinearity, i.e., a non mono-exponential intensity decay for Ficoll-400 suspensions (Figure A1), we interpret this as the formation of clusters. We model the data using

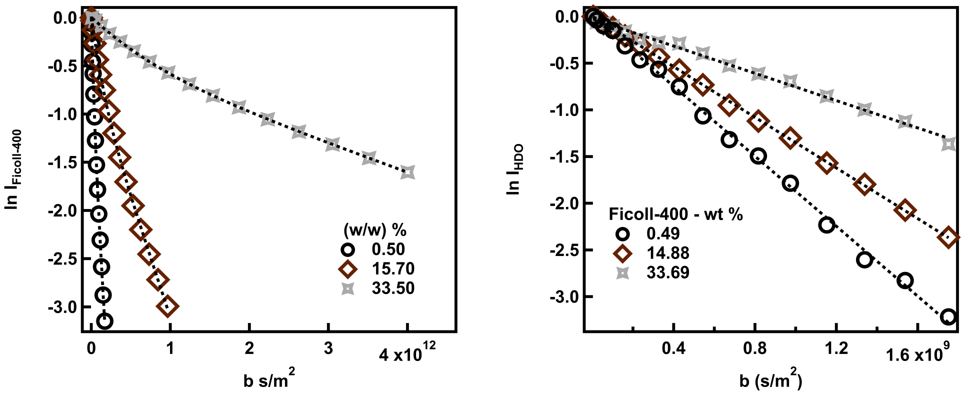

(a) (b)

Figure (A1) Representative graphs for decay of nuclear magnetic resonance intensity as a function of gradient parameter for different concentrations of Ficoll-400 ($c_{\mathrm{F}} \approx 0.5$ %, 15% and 33% $\frac{w}{w}$ (a) Ficoll-400 signal: the data is fitted using a bi-exponential function (Equation A.1). (b) Signal of trace HDO in D_2O for the same weight fractions c_{F}: data is fitted to a monoexponential function.

a bi-exponential function of the form [84],

$$I(b)/I(0) = f_m \exp((-bD_1) + (1 - f_m)\exp(-bD_2) \tag{A.1}$$

where f_m is the fraction of isolated Ficoll-400 particle (referred to as "monomer") and D_1 is the self-diffusion coefficients of the monomer and D_2 is the mean self-diffusivity of the cluster. From the fitted values, we can compute the average diffusion coefficient

$$D_{\text{ave}} = f_m D_1 + \left(1 - f_m\right) D_2. \tag{A.2}$$

The monomer fraction obtained using a bi-exponential fit for Ficoll-400 is almost independent of the concentration as shown in Figure A2; 60% of them exist in the monomer state.

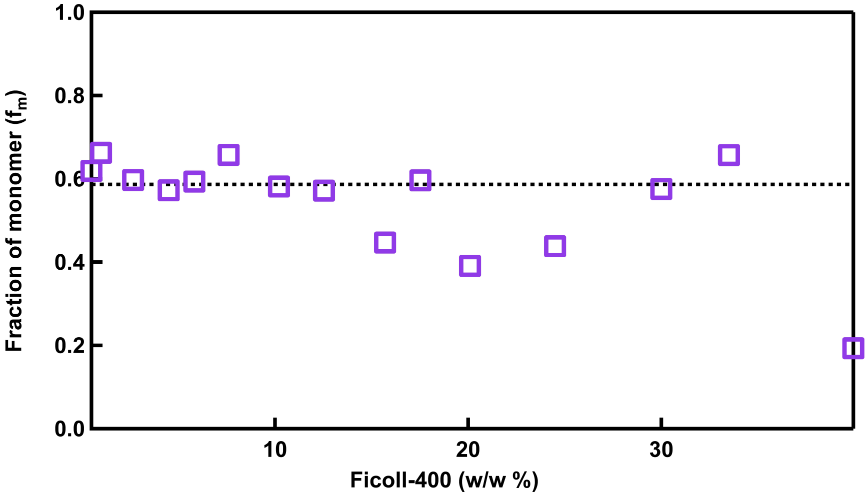

Figure (A2) The monomer fraction of Ficoll-400 is relatively independent of the concentration indicating the intrinsic polydispersity.

The HDO signal (Figure A1(b), on the other hand, is always mono-exponential, and can be fit to Equation 2.25; however the diffusivity $D^{\text{HDO}}(c_{\text{F}})$ is a function of the concentration c_{F}, as discussed in the discussion around Equation 4 in the main

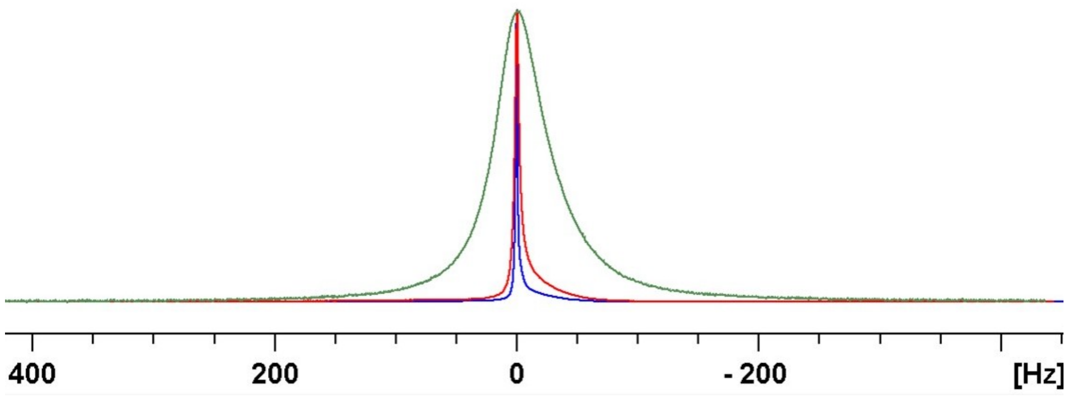

Figure (A3) ^2H D_2O spectra for D_2O in Ficoll-400: 1 % (blue line), 15 % (red line), 35 % (green line).

manuscript.

A.3 NMR transverse relaxation and ^2H NMR experiments

The Carr-Purcell-Meiboom-Gill (CPMG) pulse sequence by applying a $\frac{\pi}{2}$ pulse for a duration of 11 μs and π pulse for a duration of 22 μs with a delay time τ between the two pulses. This delay time is then varied to record the transverse relaxation intensity decay to calculate the transverse relaxation rates R_2 ($\equiv 1/T_2$).

We obtained ^2H spectra of the D_2O in Ficoll-400 at 3 concentrations (Figure A3) to verify the increase in line width that should arise from constrained motions. The spectra is recorded in deuterium channel probe.

A.4 Reduction of SANS scattering intensity from raw data

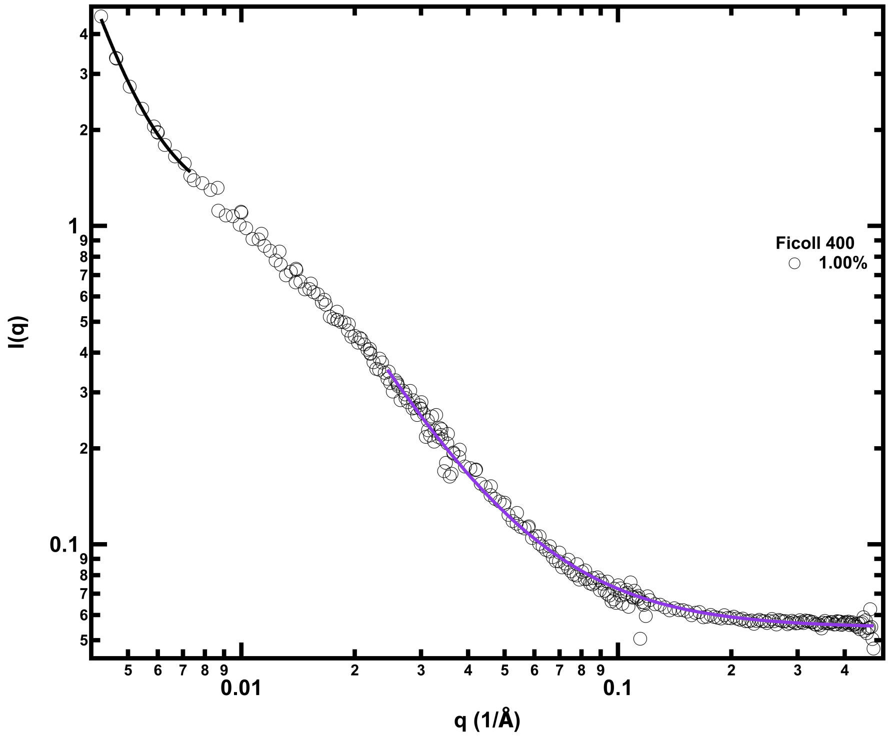

Figure (A4) Small angle neutron scattering intensity as a function of wave vector, q. The black solid line at the low q asymptote follows a -4 power law and the blue solid line at the high q asymptote follows power law of -2.

Power law fits for the high-q asymptote: Figure A4 shows the neutron scattering intensity as a function of the wave vector, q, for Ficoll 400 of 1 wt % . We extract the contribution of incoherent background scattering by fitting the high q asymptote to a power-law with a constant (solid blue line in Figure A4) of the form

$$I(q)_{\mathrm{hqa}} = A_{\mathrm{pre-factor}} q^{x} + I_{\mathrm{incoherent}}, \tag{A.3}$$

where $I(q)_{\mathrm{hqa}}$ is the intensity at high q asymptote, $A_{\mathrm{pre-factor}}$ is the prefactor, x is the power law exponent, and $I_{\mathrm{incoherent}}$ is the background incoherent scattering intensity.

We remove by subtracting the component $I_{\text{incoherent}}$ from the raw intensity. The variation of $I_{\text{incoherent}}$ (Figure A5) and $A_{\text{pre-factor}}$ (Figure A6) with Ficoll weight fraction are shown in the Appendix. The high q asymptote renders a power law of -2 and the observation holds good for all other weight fractions of Ficoll (Figure A8). The Debye function for Gaussian polymer chains predicts a -2 power law for high q asymptote, and we, therefore, first consider the Debye model to analyse our processed neutron scattering intensity data as a function of scattering wave vector.

The protons from the Ficoll contributes to the scattered background intensity and therefore the incoherent background intensity scales linearly with increase in concentration as shown in Figure A5. This is consistent with a linear increase in protonated Ficoll.

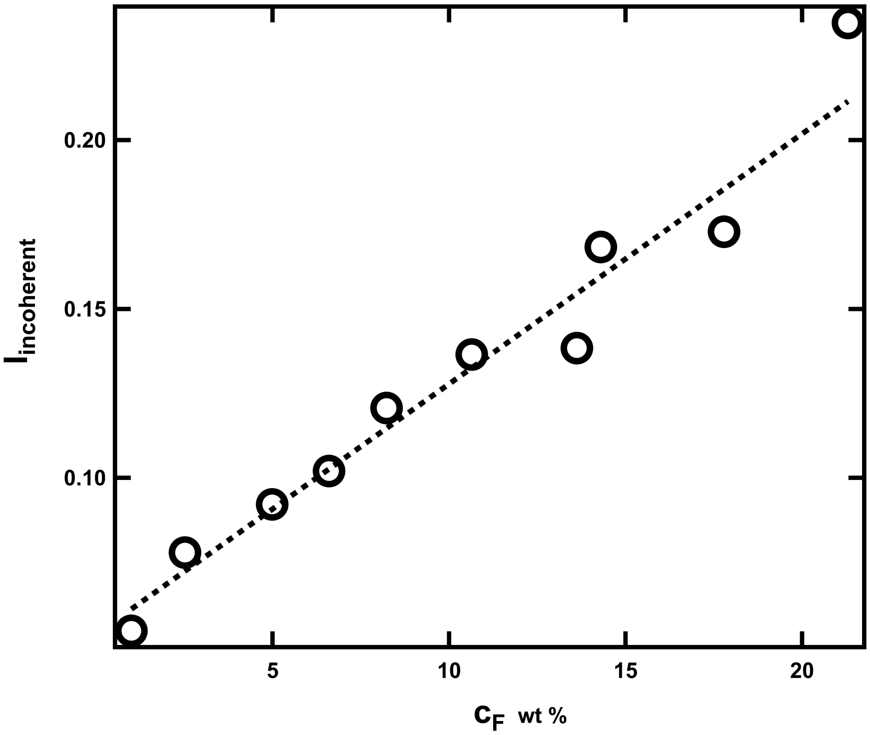

Figure (A5) The incoherent background scattering intensity extracted from the high q asymptote of the raw neutron scattering data by fitting to $I(q) = Aq^x + I_{\text{bck}}$ as a function of Ficoll 400 weight fraction.

The prefactor for the power law (Equation A.3) with the incoherent background fit to the high q asymptote scales linearly up to a concentration c less than 10 wt % and deviates from linearity with further increase in concentrations as shown in Figure A6. Coincidentally, beyond this concentration regime cluster formation in Ficoll is reported [84].

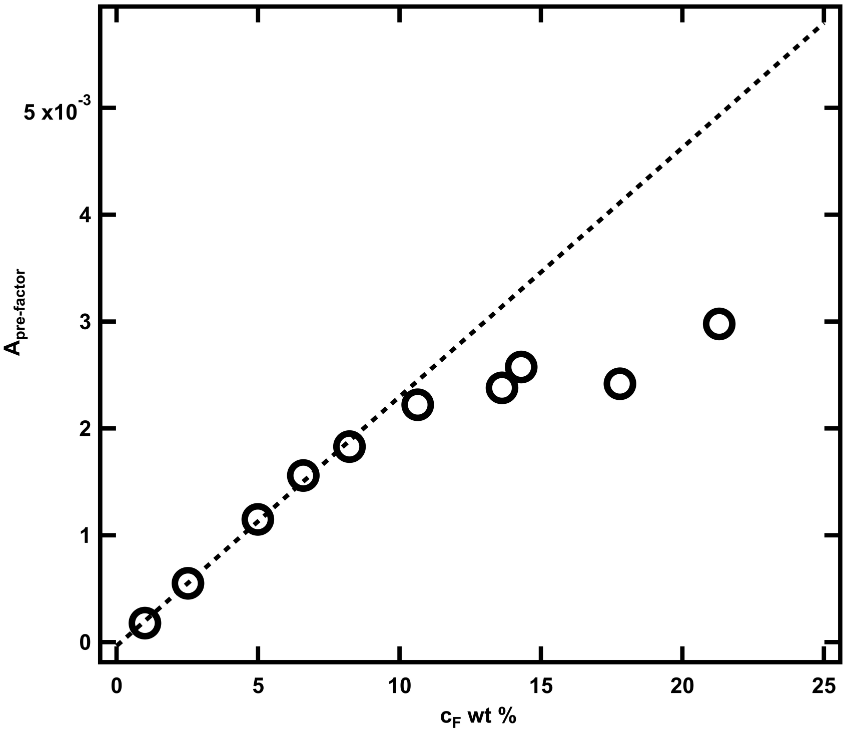

Figure (A6) The prefactor extracted for the high q asymptote of the raw neutron scattering data by fitting to Equation A.3 as a function of Ficoll 400 weight fraction.

Background and bubble contributions: Porod's law predicts a -4 power law for the scattering from a smooth spherical surface [125]. Interestingly, for at low q, we observe an intensity that appears to drop off as a power law intensity fall: we fit this low-q behaviour to

$$I(q)_{\mathrm{lqa}} = A_{\mathrm{bubble}} q^{x} + I_{\mathrm{base}}, \tag{A.4}$$

where $I(q)_{\mathrm{lqa}}$ is the intensity at the low q asymptote, A_{bubble} represents the micro

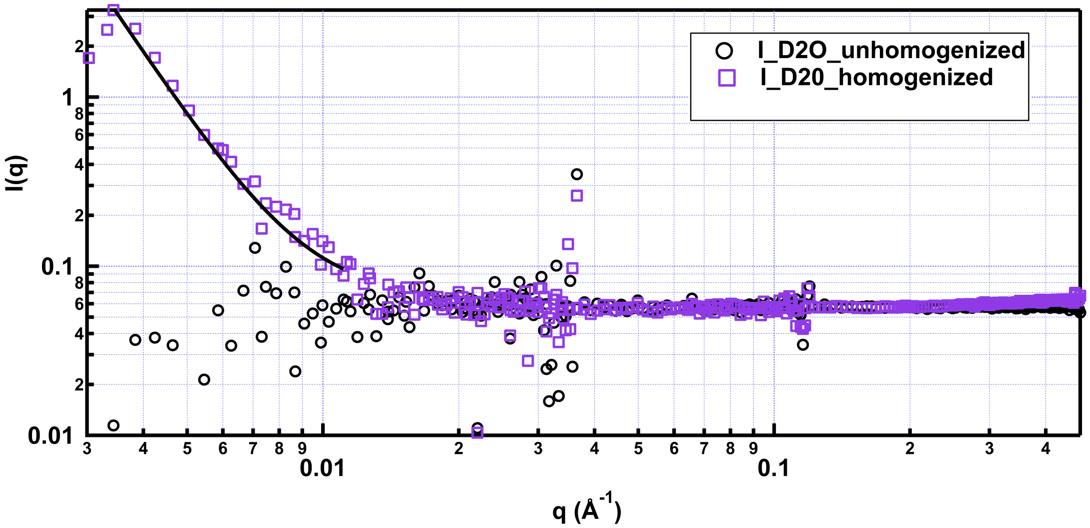

Figure (A7) Neutron scattering intensity as a function of scattering vector, q, for unhomogenized and homogenized D_2O . The fall in intensity for homogenized sample at low q asymptote follows a -4 power law indicating the presence of bubbles.

bubble factor and I_{base} is the intensity at which the scattering intensity becomes independent of the wave vector between the low q and high q asymptote. Here, the power law exponent is -4.

To verify that the fall in intensity at low q arises from the scattering from micro-bubbles in the sample, we carry out a test as follows. While a homogenized D_2O shows a power law fall in intensity with exponent -4 at the low q asymptote shown in Figure A7, an unhomogenized D_2O does not show a q dependent intensity fall. This indicates that the power law decrease in intensity at the low q asymptote in homogenized D_2O /samples arises from the presence of micro bubbles in the sample as predicted by Porod's law [125].

Figure A8 shows the raw scattering intensity with fits to both the low-q and high-q asymptote. Figure A9(a) and (b) shows the scaling of A_{bubble} and I_{base} respectively (Equation A.4) with increase in Ficoll-400 weight fraction. We remove the contribution of micro-bubbles by subtracting the power law component from the background

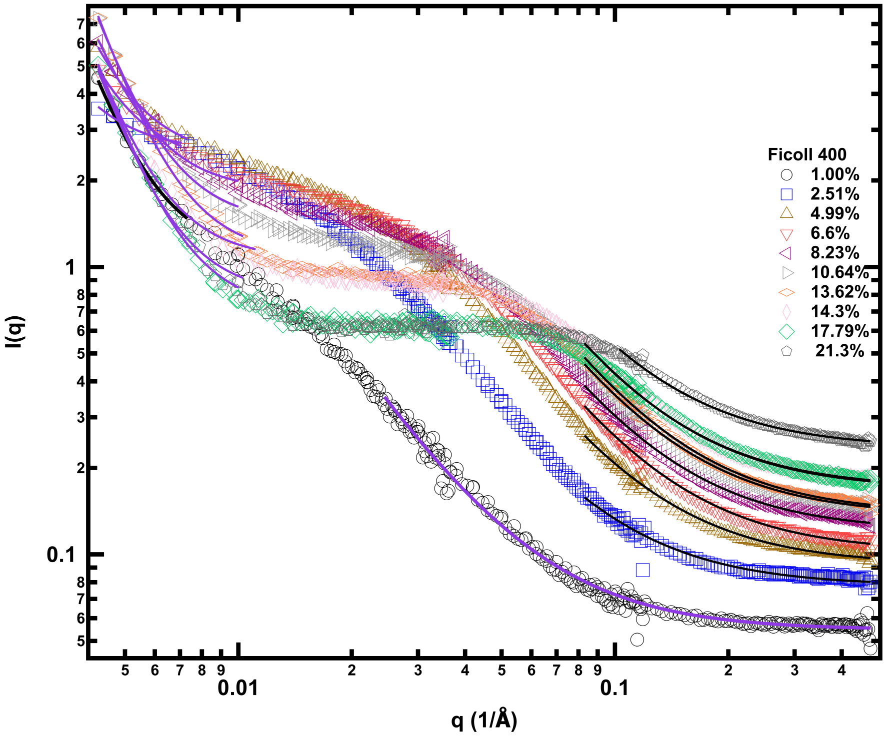

Figure (A8) Blue solid lines (low q asymptote) are the fit to $I(q) = A_{\text{bubble}} q^x + I_{\text{base}}$ (Equation A.4) and black solid lines (high q asymptote) are fits to $I(q) = Aq^x + I_{\text{incoherent}}$ (Equation A.3). The low-q asymptote follows a -4 power law and high-q asymptote follows a -2 power law.

corrected data. Figure 3.2 in the chapter 3 shows neutron scattering intensity that is devoid of scattering from micro-bubbles and incoherent background scattering for a concentrations, $c_{\text{F}} = 1\ \% \ \frac{w}{w}$, of Ficoll 400 normalized against volume fraction.

We first prepared Ficoll 400 of concentration $c_{\text{F}} = 13.62\%\ w/w$ and diluted the sample to obtain other weight fractions. The next batch was prepared at a concentration of $c_{\text{F}} = 21.3$ wt % and diluted to obtain samples until c_{F} 14.3 wt % Ficoll 400. Therefore, from $c_{\text{F}} = 13.62$ % to 1 wt %, the prefactor of the -4 power law term (that represents the fraction of bubbles) decreases. The concentration of micro-bubbles in $c_{\text{F}} = 21.3$ wt % is less than at $c_{\text{F}} = 13.62$ wt % and it decreases as we dilute the sample up to a concentration of $c_{\text{F}} = 14.3$ wt % as shown in Figure A9(a).

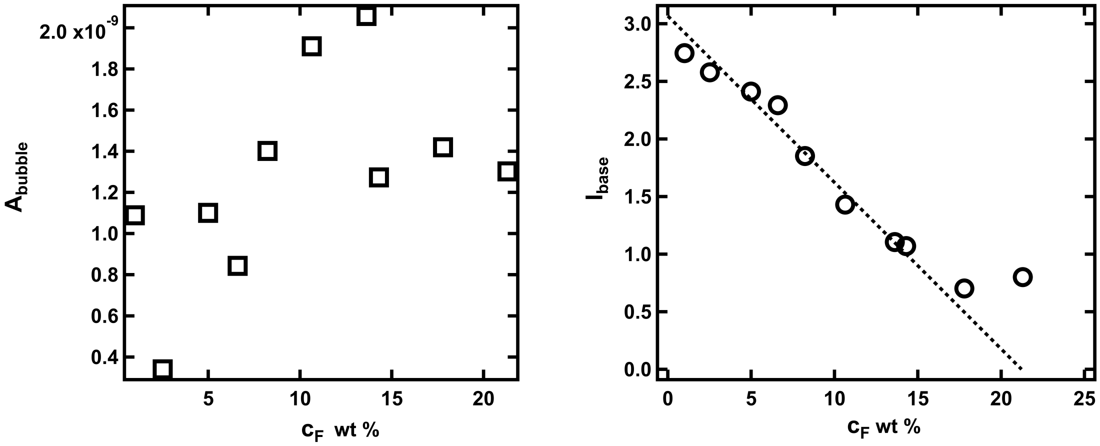

Figure (A9) (a) Bubble factor as a function of Ficoll weight fraction obtained by fitting low q asymptote to $I(q) = A_{\text{bubble}}q^x + I_{\text{base}}$. (b) The scattering intensity at $q = 0$ as a function of Ficoll weight fraction obtained by fitting low q asymptote to $I(q) = A_{\text{bubble}}q^x + I_{\text{base}}$

The scattering intensity at $q = 0$ decreases almost linearly up to a concentration of $c_F = 17.3$ % w/w and then saturates. This might indicate that the system begins approaching the crowding limit beyond 17.3 % w/w.

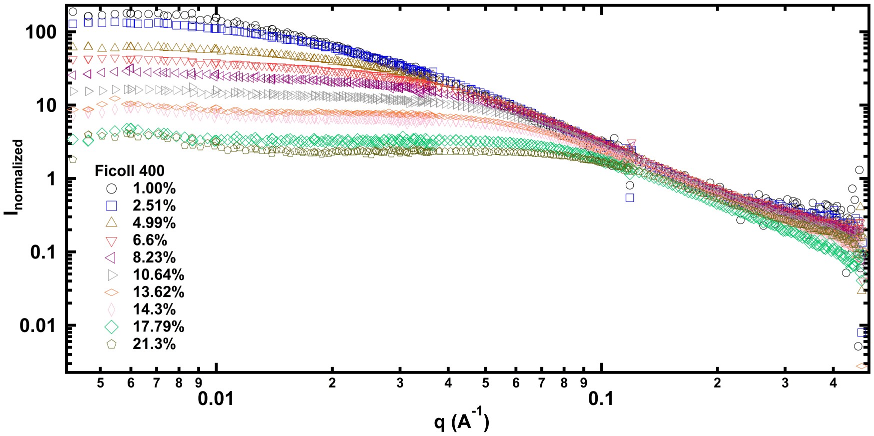

Figure (A10) (a) Neutron scattering intensity from Ficoll samples, $I(c_F)$, after removing the contribution of micro bubbles and background scattering for different suspensions investigated here.

A.5 Radius of gyration from the extended Debye–Anderson–Brumberger form factor model

The extended Debye–Anderson–Brumberger form factor model for form factor renders a form of

$$P(q) = \frac{I(q)}{I_0} = \frac{1}{\left[1 + \left[\frac{D+1}{3}\right](Rq)^2\right]^{(\frac{D}{2})}} \tag{A.5}$$

If we let $\alpha = \frac{D+1}{3}$, $\beta = \frac{D}{2}$, then

$$P(q) = \frac{1}{[1 + \alpha(qR)^2]^{\beta}}, \tag{A.6}$$

which for small x gives

$$P(q) \sim 1 - \alpha\beta(qR)^2 + O((qR)^4). \tag{A.7}$$

The Guinier approximation $\frac{I}{I_0} = \exp(\frac{-q^2R_g^2}{3})$ at small qR_g can be expanded as

$$P(q) \sim 1 - \frac{q^2{R_g}^2}{3}. \tag{A.8}$$

Comparing the prefactors of q^2 in equation A.7 and equation A.8

$$R_g = \sqrt{3\alpha\beta}R, \tag{A.9}$$

substituting the values $\alpha = 1.07 \pm 0.02$ and $\beta = 1.105 \pm 0.03$, calculated using the fit parameter D = 2.21 ± 0.05, and using the fitted R = 6.79 ± 0.03 nm from the extended Debye–Anderson–Brumberger model fit to the Ficoll form factor (Figure 3.2), we estimate an R_g of 12.78 ± 0.08 nm.

Bibliography

[1] Robert J Hunter. *Foundations of colloid science*. Oxford university press, 2001.

[2] Mark Kac. “Random walk and the theory of Brownian motion”. In: *The American Mathematical Monthly* 54.7P1 (1947), pp. 369–391.

[3] Leland H Hartwell et al. “From molecular to modular cell biology”. In: *Nature* 402.6761 (1999), pp. C47–C52.

[4] Richard Anthony Lewis Jones, Richard AL Jones, R Jones, et al. *Soft condensed matter*. Vol. 6. Oxford University Press, 2002.

[5] Rob Phillips et al. *Physical Biology of the Cell*. Garland Science, 2012.

[6] P Ziherl. *Physics of Soft Matter*. http://www-f1.ijs.si/ ziherl/smt.pdf, online lecture notes, 2013.

[7] V Adrian Parsegian. *Van der Waals forces: a handbook for biologists, chemists, engineers, and physicists*. Cambridge university press, 2005.

[8] Aleksandar Vacic et al. “Determination of molecular configuration by debye length modulation”. In: *Journal of the American Chemical Society* 133.35 (2011), pp. 13886–13889.

[9] V Arrighi et al. “Conformation of cyclics and linear chain polymers in bulk by SANS”. In: *Macromolecules* 37.21 (2004), pp. 8057–8065.

[10] Karl F Freed. “Concentration dependence of the viscoelastic properties of polymer solutions and suspensions”. In: *Ferroelectrics* 30.1 (1980), pp. 277–287.

[11] Roland G Winkler, Dmitry A Fedosov, and Gerhard Gompper. “Dynamical and rheological properties of soft colloid suspensions”. In: *Current Opinion in Colloid & Interface Science* 19.6 (2014), pp. 594–610.

[12] Michael Rubinstein, Ralph H Colby, et al. *Polymer Physics*. Vol. 23. Oxford university press New York, 2003.

[13] M Daoud et al. “Solutions of flexible polymers. Neutron experiments and interpretation”. In: *Macromolecules* 8.6 (1975), pp. 804–818.

[14] R Tuinier et al. “Concentration and shear-rate dependence of the viscosity of an exocellular polysaccharide”. In: *Biopolymers: Original Research on Biomolecules* 50.6 (1999), pp. 641–646.

[15] PG De Gennes. “Dynamics of entangled polymer solutions. II. Inclusion of hydrodynamic interactions”. In: *Macromolecules* 9.4 (1976), pp. 594–598.

[16] J. A. Cohen et al. “A phenomenological one-parameter equation of state for osmotic pressures of PEG and other neutral flexible polymers in good solvents”. In: *The Journal of Physical Chemistry B* 113.12 (2009), p. 3709.

[17] John Harding. “Biochemistry Epidemiology and Pharmacology”. In: *Cataract* (1991), pp. 195–217.

[18] R John Ellis. “Macromolecular crowding: an important but neglected aspect of the intracellular environment”. In: *Current Opinion in Structural Biology* 11.1 (2001), pp. 114–119.

[19] Paul A Srere. “The infrastructure of the mitochondrial matrix”. In: *Trends in Biochemical Sciences* 5.5 (1980), pp. 120–121.

[20] R John Ellis. “Macromolecular crowding: obvious but underappreciated”. In: *Trends in Biochemical Sciences* 26.10 (2001), pp. 597–604.

[21] Jay R Wenner and Victor A Bloomfield. “Crowding effects on EcoRV kinetics and binding”. In: *Biophysical Journal* 77.6 (1999), pp. 3234–3241.

[22] Allen P Minton. “The influence of macromolecular crowding and macromolecular confinement on biochemical reactions in physiological media”. In: *Journal of Biological Chemistry* 276.14 (2001), pp. 10577–10580.

[23] Germán Rivas and Allen P Minton. “Macromolecular crowding in vitro, in vivo, and in between”. In: *Trends in Biochemical Sciences* 41.11 (2016), pp. 970–981.

[24] Irina M Kuznetsova, Konstantin K Turoverov, and Vladimir N Uversky. “What macromolecular crowding can do to a protein”. In: *International journal of molecular sciences* 15.12 (2014), pp. 23090–23140.

[25] Germán Rivas, Frank Ferrone, and Judith Herzfeld. *Life in a crowded world: Workshop on the Biological Implications of Macromolecular Crowding.* 2004.

[26] Loren Stagg et al. “Molecular crowding enhances native structure and stability of α/β protein flavodoxin”. In: *Proceedings of the National Academy of Sciences* 104.48 (2007), pp. 18976–18981.

[27] Jörgen Ådén and Pernilla Wittung-Stafshede. “Folding of an unfolded protein by macromolecular crowding in vitro”. In: *Biochemistry* 53.14 (2014), pp. 2271–2277.

[28] Swomitra Palit et al. “Combining diffusion NMR and small-angle neutron scattering enables precise measurements of polymer chain compression in a crowded environment”. In: *Physical Review Letters* 118.9 (2017), p. 097801.

[29] Jaeoh Shin, Andrey G Cherstvy, and Ralf Metzler. “Kinetics of polymer looping with macromolecular crowding: effects of volume fraction and crowder size”. In: *Soft Matter* 11.3 (2015), pp. 472–488.

[30] Nobuhiro Muramatsu and Allen P Minton. “Tracer diffusion of globular proteins in concentrated protein solutions”. In: *Proceedings of the National Academy of Sciences* 85.9 (1988), pp. 2984–2988.

[31] Swomitra Palit et al. “The effect of crowder charge in a model polymer–colloid system for macromolecular crowding: Polymer structure and dynamics”. In: *The Journal of Chemical Physics* 147.11 (2017), p. 114902.

[32] Alexander Christiansen et al. “Factors defining effects of macromolecular crowding on protein stability: an in vitro/in silico case study using cytochrome c”. In: *Biochemistry* 49.31 (2010), pp. 6519–6530.

[33] Alexander P Schlesinger et al. “Macromolecular crowding fails to fold a globular protein in cells”. In: *Journal of the American Chemical Society* 133.21 (2011), pp. 8082–8085.

[34] Hue Sun Chan and Ken A Dill. “Intrachain loops in polymers: Effects of excluded volume”. In: *The Journal of Chemical Physics* 90.1 (1989), pp. 492–509.

[35] René Messina et al. “Overcharging: The crucial role of excluded volume”. In: *EPL (Europhysics Letters)* 60.3 (2002), p. 383.

[36] Cameron F Abrams and Kurt Kremer. “Effects of excluded volume and bond length on the dynamics of dense bead-spring polymer melts”. In: *The Journal of Chemical Physics* 116.7 (2002), pp. 3162–3165.

[37] Fabio Ganazzoli, Roberto La Ferla, and Giuseppina Raffaini. “Intramolecular dynamics of dendrimers under excluded-volume conditions”. In: *Macromolecules* 34.12 (2001), pp. 4222–4228.

[38] Hugo Hernandez. “Clausius’ sphere of action for different intermolecular potentials”. In: *ForsChem Research Reports* 10 (2017).

[39] Damien Hall and Allen P Minton. “Macromolecular crowding: qualitative and semiquantitative successes, quantitative challenges”. In: *Biochimica et Biophysica Acta (BBA)-Proteins and Proteomics* 1649.2 (2003), pp. 127–139.

[40] Allen P Minton. “A molecular model for the dependence of the osmotic pressure of bovine serum albumin upon concentration and pH”. In: *Biophysical Chemistry* 57.1 (1995), pp. 65–70.

[41] Huan-Xiang Zhou, Germán Rivas, and Allen P Minton. “Macromolecular crowding and confinement: biochemical, biophysical, and potential physiological consequences”. In: *Annu. Rev. Biophys.* 37 (2008), pp. 375–397.

[42] Farai I Rusinga and David D Weis. “Soft interactions and volume exclusion by polymeric crowders can stabilize or destabilize transient structure in disordered proteins depending on polymer concentration”. In: *Proteins: Structure, Function, and Bioinformatics* 85.8 (2017), pp. 1468–1479.

[43] Saikat Biswas et al. “Mixed macromolecular crowding: a protein and solvent perspective”. In: *ACS Omega* 3.4 (2018), pp. 4316–4330.

[44] William H Fissell et al. “Ficoll is not a rigid sphere”. In: *American Journal of Physiology-Renal Physiology* 293.4 (2007), F1209–F1213.

[45] Bert van den Berg et al. “Macromolecular crowding perturbs protein refolding kinetics: implications for folding inside the cell”. In: *The EMBO journal* 19.15 (2000), pp. 3870–3875.

[46] Bing-Rui Zhou et al. “Mixed macromolecular crowding inhibits amyloid formation of hen egg white lysozyme”. In: *Biochimica et Biophysica Acta (BBA)-Proteins and Proteomics* 1784.3 (2008), pp. 472–480.

[47] Ana Diniz et al. “Protein–glycan quinary interactions in crowding environment unveiled by NMR spectroscopy”. In: *Chemistry–A European Journal* 23.53 (2017), pp. 13213–13220.

[48] Felix Roosen-Runge et al. “Protein self-diffusion in crowded solutions”. In: *Proceedings of the National Academy of Sciences* 108.29 (2011), pp. 11815–11820.

[49] Prasad S Sarangapani et al. “The limitations of an exclusively colloidal view of protein solution hydrodynamics and rheology”. In: *Biophysical Journal* 105.10 (2013), pp. 2418–2426.

[50] Prasad S Sarangapani et al. “Critical examination of the colloidal particle model of globular proteins”. In: *Biophysical Journal* 108.3 (2015), pp. 724–737.

[51] Jonathan D Nickels et al. “Structure and hydration of highly-branched, monodisperse phytoglycogen nanoparticles”. In: *Biomacromolecules* 17.3 (2016), pp. 735–743.

[52] H Pfeifer. “A short history of nuclear magnetic resonance spectroscopy and of its early years in Germany”. In: *Magnetic Resonance in Chemistry* 37.13 (1999), S154–S159.

[53] Paul C Lauterbur. “Image formation by induced local interactions: examples employing nuclear magnetic resonance”. In: *Nature* 242.5394 (1973), pp. 190–191.

[54] Raymond Damadian. *Apparatus and method for detecting cancer in tissue.* US Patent 3,789,832. Feb. 1974.

[55] Allen N Garroway, Peter K Grannell, and Peter Mansfield. “Image formation in NMR by a selective irradiative process”. In: *Journal of Physics C: Solid State Physics* 7.24 (1974), p. L457.

[56] James Keeler. *Understanding NMR spectroscopy.* John Wiley & Sons, 2011.

[57] *Inversion recovery pulse sequence.* `https://warwick.ac.uk/fac/sci/physics/research/condensedmatt/imr_cdt/students/stephen_day/relaxation/`.

[58] Malcolm H Levitt. *Spin dynamics: basics of nuclear magnetic resonance.* John Wiley & Sons, 2013.

[59] *Pulsed field gradient NMR pulse sequence.* `http://chem.ch.huji.ac.il/nmr/techniques/other/diff/diff.html`.

[60] Paul T Callaghan. *Principles of nuclear magnetic resonance microscopy.* Oxford University Press on Demand, 1993.

[61] Timothy DW Claridge. *High-resolution NMR techniques in organic chemistry.* Vol. 27. Elsevier, 2016.

[62] I Swan et al. “Sample convection in liquid-state NMR: why it is always with us, and what we can do about it”. In: *Journal of Magnetic Resonance* 252 (2015), pp. 120–129.

[63] Geir Humborstad Sørland et al. “Improved convection compensating pulsed field gradient spin-echo and stimulated-echo methods”. In: *Journal of Magnetic Resonance* 142.2 (2000), pp. 323–325.

[64] A Guinier. “Small-Angle X-Ray Diffraction; Application to the Study of Ultramicroscopic Phenomena”. In: *Ann. Phys.(Paris)* 12.1 (1939), pp. 161–237.

[65] I Grillo. “13 Small-Angle Neutron Scattering and Applications in Soft Condensed Matter”. In: (2008).

[66] Yuri B Melnichenko and George D Wignall. “Small-angle neutron scattering in materials science: Recent practical applications”. In: *Journal of Applied Physics* 102.2 (2007), p. 3.

[67] HB Stuhrmann. “Neutron small-angle scattering of biological macromolecules in solution”. In: *Journal of Applied Crystallography* 7.2 (1974), pp. 173–178.

[68] Boualem Hammouda. “Probing nanoscale structures-the sans toolbox”. In: *National Institute of Standards and Technology* (2008), pp. 1–717.

[69] CJ Glinka et al. “The 30 m small-angle neutron scattering instruments at the National Institute of Standards and Technology”. In: *Journal of Applied Crystallography* 31.3 (1998), pp. 430–445.

[70] Steven R Kline. “Reduction and analysis of SANS and USANS data using IGOR Pro”. In: *Journal of Applied Crystallography* 39.6 (2006), pp. 895–900.

[71] *SANS Data Reduction Tutorial.* `https://www.ncnr.nist.gov/programs/sans/data/data_red.html`. 2006.

[72] Sow-Hsin Chen. “Small angle neutron scattering studies of the structure and interaction in micellar and microemulsion systems”. In: *Annual Review of Physical Chemistry* 37.1 (1986), pp. 351–399.

[73] Fabrice Cousin. “Small angle neutron scattering”. In: *EPJ Web of Conferences.* Vol. 104. EDP Sciences. 2015, p. 01004.

[74] John R. Ellis. "Macromolecular crowding: Obvious but underappreciated". In: *Trends in Biochemical Sciences* 26.10 (2001), pp. 597–604.

[75] Allen P Minton. "Excluded volume as a determinant of protein structure and stability". In: *Biophysical Journal* 32.1 (1980), p. 77.

[76] Huan Xiang Zhou, German Rivas, and Allen P. Minton. "Macromolecular crowding and confinement: biochemical, biophysical, and potential physiological consequences". In: *Annual Review of Biophysics* 37 (2008), pp. 375–397.

[77] PN Lavrenko, OI Mikryukova, and SA Didenko. "Hydrodynamic properties and the shape of the molecules of the polysaccharide Ficoll-400 in solution". In: *Polymer Science USSR* 28.3 (1986), pp. 576–584.

[78] A. P. Minton. "Models for excluded volume interaction between an unfolded protein and rigid macromolecular cosolutes: macromolecular crowding and protein stability revisited". In: *Biophysical Journal* 88 (2005), p. 971.

[79] Daniele Venturoli and Bengt Rippe. "Ficoll and dextran vs. globular proteins as probes for testing glomerular permselectivity: effects of molecular size, shape, charge, and deformability". In: *American Journal of Physiology-Renal Physiology* 288.4 (2005), F605–F613.

[80] Adedayo A Fodeke and Allen P Minton. "Quantitative characterization of polymer- polymer, protein- protein, and polymer- protein interaction via tracer sedimentation equilibrium". In: *The Journal of Physical Chemistry B* 114.33 (2010), pp. 10876–10880.

[81] Alexander Christiansen and Pernilla Wittung-Stafshede. "Quantification of excluded volume effects on the folding landscape of Pseudomonas aeruginosa apoazurin in vitro". In: *Biophysical Journal* 105.7 (2013), pp. 1689–1699.

[82] Gita Shah and Paul L Dubin. "Adsorptive interaction of Ficoll standards with porous glass size-exclusion chromatography columns". In: *Journal of Chromatography A* 693.2 (1995), pp. 197–203.

[83] Yingfan Wang and Paul L Dubin. "Observation of Ficoll charge using size-exclusion chromatography". In: *Journal of Chromatography A* 800.2 (1998), pp. 181–185.

[84] Swomitra Palit and Anand Yethiraj. "Dynamics and cluster formation in charged and uncharged Ficoll70 solutions". In: *The Journal of Chemical Physics* 147.7 (2017), p. 074901.

[85] Zaineb Aouissi et al. "Temperature study of Ficoll400 aqueous solutions, evidence of bad solvent around 35 C". In: *Journal of Molecular Liquids* 241 (2017), pp. 435–446.

[86] L Andrew Lyon and Alberto Fernández-Nieves. "The polymer/colloid duality of microgel suspensions". In: *Annu. Rev. Phys. Chem.* 63 (2012), pp. 25–43.

[87] Anna Stradner and Peter Schurtenberger. "Potential and limits of a colloid approach to protein solutions". In: *Soft Matter* (2020).

[88] PG De Gennes. "Dynamics of entangled polymer solutions. II. Inclusion of hydrodynamic interactions". In: *Macromolecules* 9.4 (1976), pp. 594–598.

[89] Luis C Acosta et al. "Large cosolutes, small cosolutes, and dihydrofolate reductase activity". In: *Protein Science* 26.12 (2017), pp. 2417–2425.

[90] PN Lavrenko, OI Mikryukova, and SA Didenko. "Hydrodynamic properties and the shape of the molecules of the polysaccharide Ficoll-400 in solution". In: *Polymer Science USSR* 28.3 (1986), pp. 576–584.

[91] JK Krueger and George D Wignall. “Small-angle neutron scattering from biological molecules”. In: *Neutron Scattering in Biology*. Springer, 2006, pp. 127–160.

[92] Stephen D Hudson et al. “Characterization of anisotropic poly (vinyl alcohol) hydrogel by small-and ultra-small-angle neutron scattering”. In: *The Journal of chemical physics* 130.3 (2009), p. 034903.

[93] Burkhard Dünweg et al. “Corrections to scaling in the hydrodynamic properties of dilute polymer solutions”. In: *The Journal of Chemical Physics* 117.2 (2002), pp. 914–924.

[94] Suliman Barhoum, Swomitra Palit, and Anand Yethiraj. “Diffusion NMR studies of macromolecular complex formation, crowding and confinement in soft materials”. In: *Progress in Nuclear Magnetic Resonance Spectroscopy* 94 (2016), pp. 1–10.

[95] Manfred Holz and H Weingartner. “Calibration in accurate spin-echo self-diffusion measurements using 1H and less-common nuclei”. In: *Journal of Magnetic Resonance (1969)* 92.1 (1991), pp. 115–125.

[96] P Venema et al. “The effective self-diffusion coefficient of solvent molecules in colloidal crystals”. In: *Journal of Colloid and Interface Science* 141.2 (1991), pp. 360–373.

[97] MH Blees and JC Leyte. “The effective translational self-diffusion coefficient of small molecules in colloidal crystals of spherical particles”. In: *Journal of Colloid and Interface Science* 166.1 (1994), pp. 118–127.

[98] Suhad Sbeih et al. “Structural parameters of soft PNIPAM microgel particles as a function of crosslink density”. In: *Journal of Colloid and Interface Science* 552 (2019), pp. 781–793.

[99] Suhad Sbeih et al. “2H NMR Study of Polymer Segmental Dynamics at Varying Cross-Linking in Poly (N-isopropylacrylamide) Microgels”. In: *Langmuir* 37.46 (2021), pp. 13664–13675.

[100] Apratim Dhar et al. “Structure, function, and folding of phosphoglycerate kinase are strongly perturbed by macromolecular crowding”. In: *Proceedings of the National Academy of Sciences* 107.41 (2010), pp. 17586–17591.

[101] Jiang Hong and Lila M Gierasch. “Macromolecular crowding remodels the energy landscape of a protein by favoring a more compact unfolded state”. In: *Journal of the American Chemical Society* 132.30 (2010), pp. 10445–10452.

[102] Gary J Pielak and Andrew C Miklos. “Crowding and function reunite”. In: *Proceedings of the National Academy of Sciences* 107.41 (2010), pp. 17457–17458.

[103] Chikashi Ota and Kazufumi Takano. “Behavior of bovine serum albumin molecules in molecular crowding environments investigated by raman spectroscopy”. In: *Langmuir* 32.29 (2016), pp. 7372–7382.

[104] Yaqiang Wang et al. “Disordered protein diffusion under crowded conditions”. In: *The Journal of Physical Chemistry Letters* 3.18 (2012), pp. 2703–2706.

[105] Jia Bai et al. “Macromolecular and Small Molecular Crowding Have Similar Effects on α-Synuclein Structure”. In: *ChemPhysChem* 18.1 (2017), pp. 55–58.

[106] Dalila Bendedouch and Sow Hsin Chen. “Structure and interparticle interactions of bovine serum albumin in solution studied by small-angle neutron scattering”. In: *The Journal of Physical Chemistry* 87.9 (1983), pp. 1473–1477.

[107] Andrew C Miklos et al. “Volume exclusion and soft interaction effects on protein stability under crowded conditions”. In: *Biochemistry* 49.33 (2010), pp. 6984–6991.

[108] Lisa M Charlton et al. “Residue-level interrogation of macromolecular crowding effects on protein stability”. In: *Journal of the American Chemical Society* 130.21 (2008), pp. 6826–6830.

[109] Hurmiz Shamana et al. “Unusual polysaccharide rheology of aqueous dispersions of soft phytoglycogen nanoparticles”. In: *Soft Matter* 14.31 (2018), pp. 6496–6505.

[110] U Gasser et al. “Form factor of pNIPAM microgels in overpacked states”. In: *J. Chem. Phys.* 141.3 (2014), p. 034901.

[111] Bruce Alberts et al. *Essential cell biology.* Garland Science, 2015.

[112] Masahiro Kinoshita. “Roles of entropic excluded-volume effects in colloidal and biological systems: Analyses using the three-dimensional integral equation theory”. In: *Chemical Engineering Science* 61.7 (2006), pp. 2150–2160.

[113] Allen P Minton. “Excluded volume as a determinant of macromolecular structure and reactivity”. In: *Biopolymers: Original Research on Biomolecules* 20.10 (1981), pp. 2093–2120.

[114] Allen P Minton. “Effect of a concentrated “inert” macromolecular cosolute on the stability of a globular protein with respect to denaturation by heat and by chaotropes: a statistical-thermodynamic model”. In: *Biophysical Journal* 78.1 (2000), pp. 101–109.

[115] Steven B Zimmerman and Allen P Minton. “Macromolecular crowding: biochemical, biophysical, and physiological consequences”. In: *Annual Review of Biophysics and Biomolecular Structure* 22.1 (1993), pp. 27–65.

[116] Bert van den Berg, R John Ellis, and Christopher M Dobson. “Effects of macromolecular crowding on protein folding and aggregation”. In: *The EMBO Journal* 18.24 (1999), pp. 6927–6933.

[117] Youxing Qu and DW Bolen. “Efficacy of macromolecular crowding in forcing proteins to fold”. In: *Biophysical Chemistry* 101 (2002), pp. 155–165.

[118] Shannon L Flaugh and Kevin J Lumb. “Effects of macromolecular crowding on the intrinsically disordered proteins c-Fos and p27Kip1”. In: *Biomacromolecules* 2.2 (2001), pp. 538–540.

[119] VV Vasilevskaya et al. “Collapse of single DNA molecule in poly (ethylene glycol) solutions”. In: *The Journal of Chemical Physics* 102.16 (1995), pp. 6595–6602.

[120] Stefan Wallin. *Personal communication.*

[121] Yaakov Rosenfeld. “Relation between the transport coefficients and the internal entropy of simple systems”. en. In: *Physical Review A* 15.6 (June 1977), pp. 2545–2549. ISSN: 0556-2791. DOI: `10.1103/PhysRevA.15.2545`. URL: `http://link.aps.org/doi/10.1103/PhysRevA.15.2545` (visited on 09/13/2016).

[122] Mikhail Dzugutov. “A universal scaling law for atomic diffusion in condensed matter”. In: *Nature* 381.6578 (May 1996), pp. 137–139. ISSN: 0028-0836. DOI: `10.1038/381137a0`. URL: `http://www.nature.com/doifinder/10.1038/381137a0` (visited on 09/13/2016).

[123] Alice L. Thorneywork et al. “Effect of Hydrodynamic Interactions on Self-Diffusion of Quasi-Two-Dimensional Colloidal Hard Spheres”. en. In: *Physical Review Letters* 115.26 (Dec. 2015), p. 268301. ISSN: 0031-9007, 1079-7114. (Visited on 03/17/2016).

[124] Francesca Palombo and Daniele Fioretto. “Brillouin light scattering: applications in biomedical sciences”. In: *Chemical reviews* 119.13 (2019), pp. 7833–7847.

[125] G Porod. “Die Röntgenkleinwinkelstreuung von dichtgepackten kolloiden Systemen”. In: *Kolloid-Zeitschrift* 124.2 (1951), pp. 83–114.